UNIVERSITY OF CALIFORNIA,
IRVINE

Elastography mapping and microstructural analysis of heterogeneous materials based on wave motion

DISSERTATION

submitted in partial satisfaction of the requirements
for the degree of

DOCTOR OF PHILOSOPHY

in Civil Engineering

by

Dongxu Liu

Dissertation Committee:
Professor Lizhi Sun, Chair
Associate Professor Farzin Zareian
Associate Professor Mo Li

2020

TABLE OF CONTENTS

Page

LIST OF FIGURES

LIST OF TABLES

ACKNOWLEDGMENTS

I would like to express the deepest appreciation to my advisor, Professor *Lizhi Sun*, who conveyed an exploring spirit with respect to research and had the excellent patience and the constructive guidance toward finishing my PhD program.

I would like to thank my committee members, Professor *Farzin Zareian* and Professor *Mo Li*, for their guidance.

I would also like to thank Professor *Frithjof Kruggel* for offering a 3D head model.

VITA

Dongxu Liu

2001 B.A. in Civil Engineering, Northeast Electric Power University

2004 M.S. in Engineering Mechanics,
Institute of Mechanics, Chinese Academy of Sciences

2004-2013 Structural Engineer, Institute of Power Machine, Hohhot China

2014-2015 Research Associate, Department of Civil and Environmental Engineering, University of California, Irvine

2016-2020 Research Assistant, Department of Civil and Environmental Engineering, University of California, Irvine

2020 Ph.D. in Civil Engineering, University of California, Irvine

PUBLICATIONS

- Dongxu Liu, P. Qiao, Z. Zhou and L.Z. Sun, Microstructural origins of wave modulus of elasticity of concrete materials. Journal of Engineering Mechanics. 2020, 146(5): 04020028.
- Dongxu Liu, Zhijian Hu, Ge Wang and L.Z. Sun, Sound transmission-based elastography for mapping elasticity. IEEE Access, 2019, 7: 74383-74392.
- Q. Luo, Dongxu Liu, Pizhong Qiao, Zhidong Zhou and L.Z. Sun, Micro-CT-based micromechanics and numerical homogenization for effective elastic property of ultra-high performance concrete. International Journal of Damage Mechanics, 2020, 29(1): 45-66.
- Q. Luo, Dongxu Liu, P. Qiao, Q.G. Feng, and L.Z. Sun, Microstructural damage characterization of concrete under freeze-thaw action, International Journal of Damage Mechanics, 2018, 27(10): 1551-1568.
- Dongxu Liu, Z.D. Zhang, L.Z. Sun, Nonlinear elastic load–displacement relation for spherical indentation on rubberlike materials. Journal of Materials Research, 2010, 25(11): 2197-2202.
- T-C Shih, Jeon-Hor Chen, Dongxu Liu, et al., Computational Simulation of Breast Compression Based on Segmented Breast and Fibroglandular Tissues on Magnetic Resonance Images. Physics in Medicine and Biology, 2010, 55 (14): 4153-68.

ABSTRACT OF THE DISSERTATION

Elastography mapping and microstructural analysis of heterogeneous materials based on wave motion

By

Dongxu Liu

Doctor of Philosophy in Structural Engineering

University of California, Irvine, 2020

Professor Lizhi Sun, Chair

Elastography is of great interest in the fields of solid mechanics and biomechanics due to its nondestructive capability of mapping elasticity of materials and tissues. The elastography framework relies on external excitations which stimulate deformation inside an object. The internal response is then acquired and analyzed to map the distribution of elastic moduli. The first method developed in this dissertation is that, with no need of measuring any internal responses, an elastography method integrated with tomography is proposed, only requiring the transmitted responses of applied sound waves. During the process, the tomography image (e.g., CT or MRI) and the applied waves are integrated into a computational model. Following the principle of factorial design, elastic distribution of all phases in the object is reconstructed when the computational transmission of waves matches with the measured transmission. As an improved algorithm to the integration method, in the dissertation, deep convolutional neural networks (CNNs) are studied for mapping elastography with much less computation time. A CNNs architecture is developed, considering the contribution of raw features.

In the dissertation, another elastography method is developed by untangling the complex wave-induced strain field into the one due to pure compressional or shear disturbance. The proposed untangling method is realized according to the fact that the volumetric strain is caused by compressional waves. By transforming both the volumetric strain tensor and the general tangled strain tensor to the shear wave direction, the transient vibration velocity and strain generated by compression wave can be separated from their initial coupled fields and used to reconstruct elastography.

Nondestructive ultrasound-based methods have been applied to evaluate the elastic properties of composite materials. While the wave modulus of elasticity is frequently reported higher than the static counterpart, the microstructural and physical mechanisms are not well understood. In the dissertation, a computational micromechanics is conducted to investigate the effects of inclusions on both the effective wave modulus of elasticity and static modulus of elasticity. Taking concrete as an example, based on concrete microstructures resolved with X-ray micro-tomography. It is demonstrated that the existence of void defects plays a significant role on the elastic properties of concrete when compared with the particles that are also called aggregate. It is shown that the higher wave modulus of elasticity of concrete than the static one is caused by the existence of crack-like voids with small aspect ratios.

Chapter 1 Introduction

Who is the most general “Doctor” in hospitals? It is the “Dr. Image”. Most of departments rely on the Dr. Image to identify diseases, make treatment plans and prescribes. Since the advent of X-ray, people never stopped imaging the internal world of the human body. Medical imaging not only presents beauties of the body, but also helps to detect pathological changes. Up to date, more imaging modalities have been developed and applied in clinical practice. The most popular three types are X-ray based imaging, magnetic resonance imaging (MRI) and ultrasound imaging.

In the category of X-ray based imaging, there are four subcategories, Radiography, Fluoroscopy, Mammography and Computed tomography (CT) [1]. Radiography makes use of the mass attenuation difference in tissues and acquires the transmitted X-ray using a detector that records a superimposed projection of all tissues on the path of incidence. The X-ray transmission obeys Beer’s law of exponential attenuation [2]. With advancements in technology, this kind of radiography usually is labeled as traditional X-ray imaging. However, it is still the main imaging means at many medical facilities. Fluoroscopy plays the radiography movie that continuously acquires projections with time. As for mammography, it has better contrast using lower energies. Mammography as such is termed as the radiography of the breast. CT birth brought a revolution in the field of medical imaging that firstly resolved non-invasive cross-sectional images. Original CT detecting data are not human-readable until they are translated into 3D image with reconstruction algorithms. Currently, the studies on CT never stopped. Many remarkable and promising findings have been achieved, such as phase-contrast CT, multidetector CT, portable CT, dual-energy CT and so on [3], [4].

Unlike CT using attenuation principle, MRI exploits magnetic properties of atomic nuclei to image tissues. Because human tissues are rich in hydrogen atoms, hydrogen is usually used to generate MRI image where hydrogen atoms are aligned by a magnetic field, and then the alignments are disordered by an applied electromagnetic field. During the process, the tissues can be differentiated by monitoring the behavior of hydrogen atoms. Currently, as same as CT, all aspects around MRI have received intense investigations. Except the conventional MRI imaging, the developments in technologies and algorithms introduce more members into the MRI family with better image quality and patient safety, such as CEST-MRI (Chemical Exchange Saturation Transfer MRI), DWIBS (Diffusion-weighted Whole-body Imaging with Background body signal Suppression), compressed sensing MRI and MR fingerprinting [5], [6].

Ultrasound imaging produces the image of tissues based on the “pulse echo” mode in which the ultrasound waves from a pulser go into tissues and the reflected or scattered waves are collected by a receiver. “Ultra” means high frequency, typically in the MHz range [2]. The image contrast is attributed to the impedance difference of tissues that leads to reflection at the interfaces between tissues. In the family, Doppler ultrasound imaging using different principle has been established to visualize the blood flow in the light of the Doppler effect. Recently, ultrasound imaging has gained a new life and become a hot research area because of elastography that is another medical imaging modality. Elastography will be introduced in detail later.

Besides the three branches introduced above, there are still e few of other imaging modalities that have demonstrated their clinical utility, including nuclear medicine (NM) imaging, nuclear medicine planar imaging, single photon emission computed tomography

(SPECT), positron emission tomography (PET) [1]. Although the background introduction is very brief and touches upon just peripherally, it is noted that any one of them does not have the capacity covering the whole spectrum of imaging demands, i.e. each modality has itself features and shortages. For example, from resolution point of view, the spatial resolution of those imaging modalities is summarized in Table 1 that illustrates the clinical practice variance with different imaging technique. Therefore, one of future tendencies in medical imaging is to combine two or more modalities into one device for multipurpose identification [7], [8].

Table 1. The spatial resolution of each imaging modality *[1]*

Modality	Spatial Resolution (mm)	Comments
Screen film radiography	0.08	Limited by focal spot size and detector resolution
Digital radiography	0.17	Limited by size of detector elements and focal spot size
Fluoroscopy	0.125	Limited by detector resolution and focal spot size
Screen film mammography	0.03	Highest resolution modality in radiology, limited by same factors as in screen film radiography
Digital mammography	0.05-0.10	Limited by same factors as digital radiography
Computed tomography	0.3	About 0.5 mm pixels
Nuclear medicine planar imaging	2.5 (detector face) 5 (10 mm from detector)	Spatial resolution degrades substantially with distance from detector
Single photon emission computed tomography	7	Spatial resolution worst towards the center of cross-sectional image slice
Positron emission tomography	5	Better spatial resolution than the other nuclear imaging modalities
Magnetic resonance imaging	1.0	Resolution can improve at higher magnetic fields
Ultrasound imaging (5 MHz)	0.3	Limited by wavelength of sound

The main aim of medical imaging is to improve diagnostic ability. Elastography as a new group has drawn much attention because it shows wide application prospects in future clinical practice, being expected to map the mechanical properties of tissues just like

palpation on superficial tissues [9]–[11]. It is well known that cancerous or tumorous tissues are locally stiffer than their surroundings [12]. In many case, CT, MRI or Ultrasound cannot differentiate one tissue from another one, which can be illustrated by Fig. 1 where elastography shows the shear moduli of tissues varying by over five orders of magnitude compared with other modalities [13]. In term of Fig. 1, elastography dominantly prevails over other modalities and has the widest operation band. So those mechanical parameters, such as Young's modulus, shear modulus, strain, wave speed and wavelength, are related to mapping elastography.

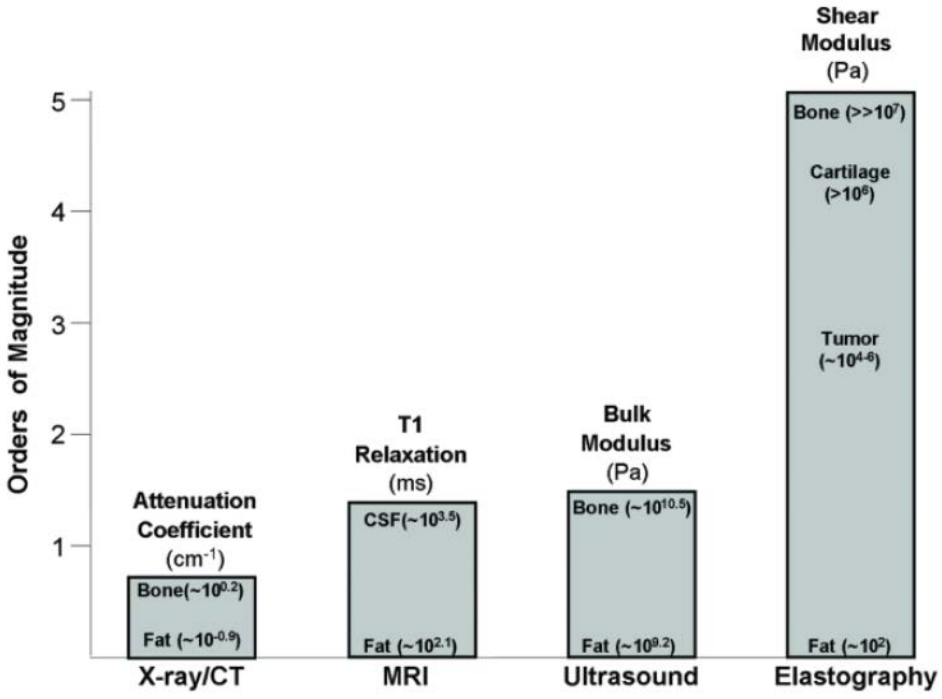

Fig. 1. The contrast comparison of imaging modalities [13]

The terminology "elastography" was firstly used in 1991, describing the stiffness distribution image [14]. Until 1997, the elastography technology was firstly used in clinical attempts for the breast lesion [15]. Due to the unique feature of elastography, the research publications on it is increasing exponentially, which can be known from the publications

statistics as shown in Fig. 2 [16]. As a positive result from those effort, ultrasound elastography has been approved for clinical use by Food and Drug Administration (FDA) [17].

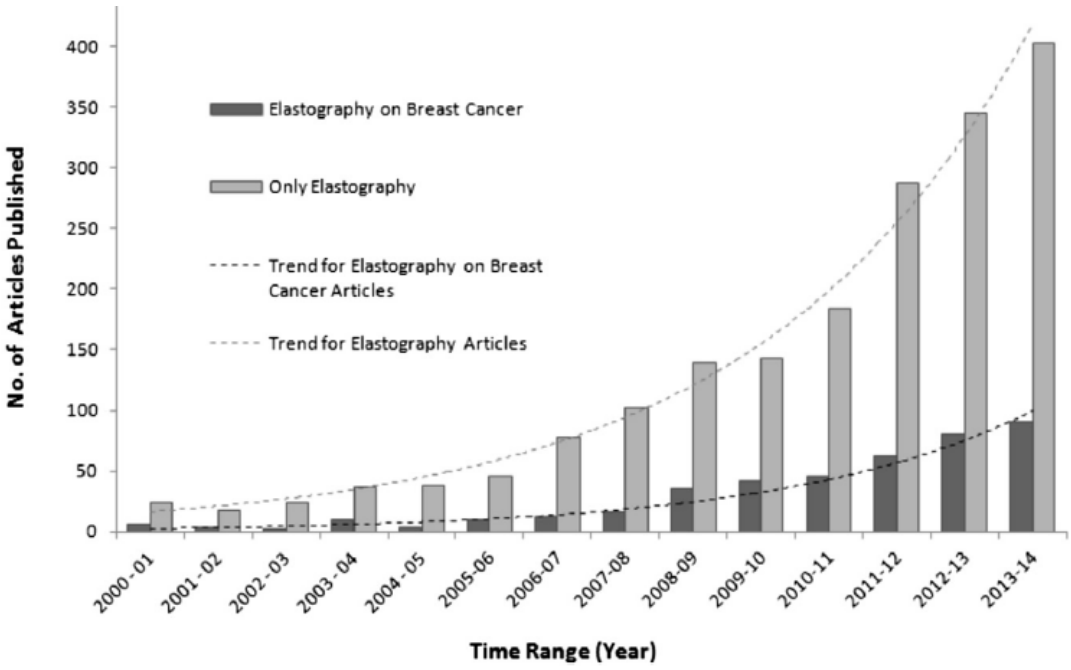

Fig. 2. The statistics of research publications for elastography [16]

In nature, elastography is to track responses to mechanical stimuli and must be with a mature imaging technology as the incubator (Ultrasound, MRI or CT). Since CT image processing puts a hurdle in synchronizing with displacement/strain measurement, CT elastography has not yet been evolved as a main direction. But, there are still pioneering works exploring and fostering the CT elastography [9], [18]. Thus, elastography can be currently divided into subfamilies: Ultrasound elastography (USE) and Magnetic Resonance Elastography (MRE). Regarding USE, some called strain elastography that depends on the displacement measurement and strain calculation according to acquired ultrasound signals generated by external compression on tissues [14], [19], [20]. Strain elastography (SE) can

only construct relative stiffness distribution image because the real stress inside tissues are not accurately estimated. A couple of algorithms has been put forward on SE. The crosscorrelation algorithm is to calculate the displacement based on the original and delayed signals [14], [21]–[23]. The decorrelation algorithm is a type of filter correcting artifacts and improving the elastogram quality [24], [25]. The envelope processing algorithm is that tissues are distinguished by estimating the upper bound of contrast-to–noise ratio [26]. Others of USE are named shear wave elastography (SWE) in which the wave length or wave speed inside tissues is estimated to predict the stiffness distribution image [27]–[32]. Why not compression waves? For soft tissues, the speed of compression waves is range of 1450~1600 m/s [1]. The stiffer materials have higher speed. It is hard to trace and measure their speed or wavelength. However, the shear wave speed is very slow, around 10 m/s, in comparison with the compression wave speed [33]. UE has been widely and successfully used to investigate and characterize the following soft tissues: breast imaging [15], [19], [29], [34]–[38], liver imaging [39]–[44], prostate imaging [45]–[47], thyroid imaging [48]–[50]. In contrast with USE, MRE is considered in the infant stage [51], and more costly and time-consuming than ultrasound elastography. However, it is still promising because MRE has the capacity of constructing the 3D image with high accuracy. Strain MRE aims to measure the internal strain incurred by quasistatically external loading [52]–[54]. Dynamic MRE predicts the modulus distribution and is realized by estimating the wavelength of the mechanical waves inside tissues [55], [56] or by a direct inversion scheme [57], [58]. Currently, leading investigations have been focused on liver MRE [59]–[62], breast MRE [63]–[66], muscle MRE [67]–[70], and brain MRE [71]–[74]. Especially, brain tissues are enclosed by three layers of cerebral meninges, cerebrospinal fluid (CSF)

and the skull which prevent the ultrasound from penetrating into the deep and isolate the inside tissues from the external excitation [13], [75]. Although the external actuation system was designed to perform MRE [72], that will bring more extra accessories for the possible clinical practice. In reality, a live brain will be never still because of the presence of arterial pulsation. Researchers are using the intrinsic pulsation as the signal source to map the mechanical parameters of the brain tissues [73], [75]–[77]. There are three milestones for the intrinsic elastography. The first is that Zhao et al (2009) measured the brain tissue velocity triggered by the blood pulsation and then fitted a damped oscillation model to predict the elasticity of the brain. Similarly, the second is that Weaver et al (2012) measured the tissue velocity at multiple phases of the cardiac cycle and integrated the velocity to obtain the displacement and then fitted the wave equation with displacement to predict the shear modulus. The third one is a signal processing method in which, taking advantage of the time-reversal and the cross-correlation method, the shear modulus was extracted from the shear waves caused by cardiac motion, blood pulsation, and any muscle activity. Because blood vessels are everywhere, the resultant modeling challenge is to cover all possible vessels that contribute to displacement in computational models. The time reversal method needs the pure shear signal which raises a new challenge of how to decode the shear wave out of shear-compressional interaction.

Not only can wave motion be applied to image elastography, but to characterize the mechanical properties of composite materials. For example, the elastic modulus of concrete can be assessed according to the measured velocity of wave propagation [78]–[82]. For homogeneous materials, it is expected that the elastic modulus measured by wave be equal to be done by the static tensile or compressive test. For composite materials are

heterogeneous, the wave motion will be affected by inclusions. So, it has been reported that WM of concrete is up to 30% higher than its corresponding static modulus of elasticity based on both longitudinal and shear wave excitations [78], [82], [83]. However, the reason causing the difference has been not understood well so far. In the study, the volume fraction, shape and types of inclusion will be investigated, and thereafter the significant reason be clarified.

In this dissertation, three elastography methods will be proposed, free of frequency dependence, independent of waveform and not limited to pure shear deformation. Transmission-based elastography will be presented in Chapter 2, deep learning CNNs powered elastography in Chapter 3 and compressional-shear deformation untangled elastography in Chapter 4. Effect of microstructures on wave propagation will be studied in Chapter 5. Summary and future research is in Chapter 6.

Chapter 2 Wave Transmission Based Elastography

2.1 Introduction

Elastography, as an emerging image modality, has drawn great attention due to its application prospect in charactering biomechanical properties, which also is expected to strengthen the diagnosis of pathological changes and predict elasticity with the nondestructive mode [9], [10], [55], [84]–[86]. It is well known that most cancerous or tumorous tissues are locally stiffer than their surroundings [12]. For example, most breast tumors confined to the ducts themselves are designated ductal carcinomas in situ (DCIS), which are the initial stage of malignant tumors. Pathological changes of these DCIS are known to be correlated with changes in tissue stiffness (modulus), resulting in extremely hard nodules. Masses form and grow because of inflammation and desmoplasia, a dense cellular reaction specific to malignant lesions with highly cross-linked collagenous fibers. In fact, the shear moduli of tissues vary over five orders of magnitude whereas other imaging modalities, CT, MRI and Ultrasound only detect tissues within two orders of magnitude as shown in Fig. 1. From this point of view, elastography is more promising in detecting cancerous tissues. Therefore, modulus-directed elastography has become an attractive tool to investigate the mechanical properties of tissues. Those mechanical parameters related to elasticity, including Young's modulus, shear modulus, strain, wave speed, and wavelength, can be used to reconstruct elastography. To this end, an external excitation on tissues/phantoms, most commonly the sound wave including continuous and transient waves, is applied to measure these parameters inside tissues.

A great deal of research efforts working on elastography with sound waves and the commercial exploration for clinical application have been reported [11], [87]–[93]. While a few anisotropic modeling works have been explored [9], [10], current efforts in the literature are dominantly in the assumption of isotropic elasticity, considering the tedious, time-consuming inverse computation and the focus on averaged identification of pathological changes. In the frame of linear elasticity some algorithms have been developed to map the elastography inversely, which are rooted in the governing equations of wave propagation in homogeneous isotropic elastic solid without the body force,

$$(\lambda + \mu)u_{j,ji} + \mu u_{i,jj} = \rho \ddot{u}_i \tag{1}$$

where λ and μ are Lamé constants (μ is also called the shear modulus), i and j are the coordinate indices ($i, j = 1,2,3$) in Cartesian tensor notation, u_j is the displacement vector, and ρ is the density of solid [94], [95]. By considering that the shear wave does not change volume, i.e., $u_{i,i} = 0$, the velocity of shear wave V_s can be derived as,

$$V_s = \sqrt{\mu/\rho} \tag{2}$$

As for continuous waves, after low-frequency shear waves are emitted into tissues by external sources, the local wavelengths are measured through either the color Doppler image or phase-contrast magnetic resonance image from which velocities are estimated and shear moduli are finally predicted based on Eq. (2) [55], [58], [84]. However, direct measurement is challenging because of irregular shapes and internal reflections of tissues. Therefore, by using Eq. (1), the model-based schemes, direct inversion and iterative inversion such as the elasticity tensor based reconstruction, the sub-zone based reconstruction, and the dynamic cardiac elastography, have been developed for continuous wave elastography [10], [57], [94], [96]. In addition, efforts coming from signal process and

correlation analysis such as the reverberant shear-wave fields frame and the time reversal based reconstruction have been made to map continuous wave elastography [92], [97], [98]. As for transient waves, pulse shear waves are generated by external sources and deform tissues locally, which makes wavelengths or wave velocities measurable by tracking wave propagation such as shear wave elasticity imaging, supersonic shear imaging and shear wave speed imaging [99]–[101]. Overall, current elastography methods heavily rely on the internal mechanical responses to the external wave excitation. For example, the wavelength or the wave speed of the tissue needs to be detected to predict the elasticity distribution, in which critical problems remain to be solved, including overcoming wave attenuation in tissues, considering the reflection and refraction of wave at interfaces, random noise effect and sophisticated image processing [11], [87], [88], [91], [92], [94]. In elastodynamics, these mechanical responses are governed by the partial differential equation (1). In most of cases, however, tissues are of multiple phases and irregular shapes, which leads to difficulty finding analytical solutions to Eq. (1). Resultantly, computational methods as an effective means, most commonly, the finite element method (FEM), have been employed to solve (1). [10], [94], [96], [102]–[105].

In the chapter, an integrated method under the framework of isotropic elasticity, referred to as the sound transmission-based elastography, is proposed, using the tomography images (e.g., CT and MRI) and transmitted wave signals at surface locations. It is remarkable that only transmitted signals through the sample, not the internal responses inside the sample, are needed for the elastography reconstruction. The image and the wave incidence are integrated into a computational model. Following a procedure of inverse analysis, elasticity distribution of all phases in the object is reconstructed when the

computational transmission converges to the measured transmission. The numerical simulation on brain tissues and the experiment on the silicon rubber phantom are conducted to validate the proposed method. Both cases illustrate that the integrated method successfully predicts the real elasticity of samples. The verification measurements on the phantom show the predicted elastic properties agree well with the experimental results of uniaxial compression testing.

2.2 Method

Wave motion inside tissue media carries the information of the mechanical properties and so does its transmission carry the same information filtered by internal structures, which is completely controlled by the governing equations (1). The tomography image resolved by CT, MRI or Ultrasound contains the tissue structure information and can identify the position and size of suspicious lesions such as cancerous or tumorous tissues. They can be integrated and simulated in a computational model with FEM in which the wave incidence of sound test serves as the external load and the image is used to generate finite-element mesh. As for the elastic modulus of each phase in FEM, it is the goal that needs to be analyzed inversely and mapped. Thus, a computational model is built, and the elastography image is reconstructed following a procedure of inverse analysis when the FEM transmission output matches with the measured transmission signals at surface locations of object.

Specifically, the first step is to obtain the object tomography to characterize the internal structure. All tissues are segmented under CT/MRI resolution. The segmented tomography serves as the two-dimensional or three-dimensional geometry input of the

inverse analysis as shown in Fig. 3. The second step is to conduct the sound-wave test on the same object used in the first step. Sound transducers are laid out on the surface of the object, some of which serve as the pulsers that fire the incident wave and others as the receivers that collect the transmitted signals. Depending on phases of a tissue that need to be mapped, the number of transducers should be enough for exciting each phase and receiving the transmission and reflection through each phase. The third step is to build a computational model based on the tomography image and the incident sound wave acted on the object. Image process may be necessary to convert image into a specific format acceptable for FEM meshing. The meshed regions are completely identical with segmented tissues in the first step. In this step, for the sake of ensuring accurate simulation, it is noted that there are at least 10 nodes representing each wavelength for whatever the element type (e.g., four-node quadrilateral elements, three-node triangular elements and 4-node tetrahedral elements) and the interpolation functions (e.g., second order shape functions) are adopted [106]. The displacement boundaries are set in terms of real conditions or without disturbing the real wave propagation when applying FEM. The fourth step is to conduct FEM simulation and inverse analysis until its output converges to measured transmission signals within the preset error as shown in Fig. 3. As for the error, there is no general threshold available because the accuracy of inverse analysis is influenced by many factors such as signal noise, image noise, algorithms, numerical error, computation time, and so on. In practice, it could be determined empirically and be helpful to test the noise level in advance. The third and the fourth steps form a calculating loop in which the fourth one provides the parameter update for the third step.

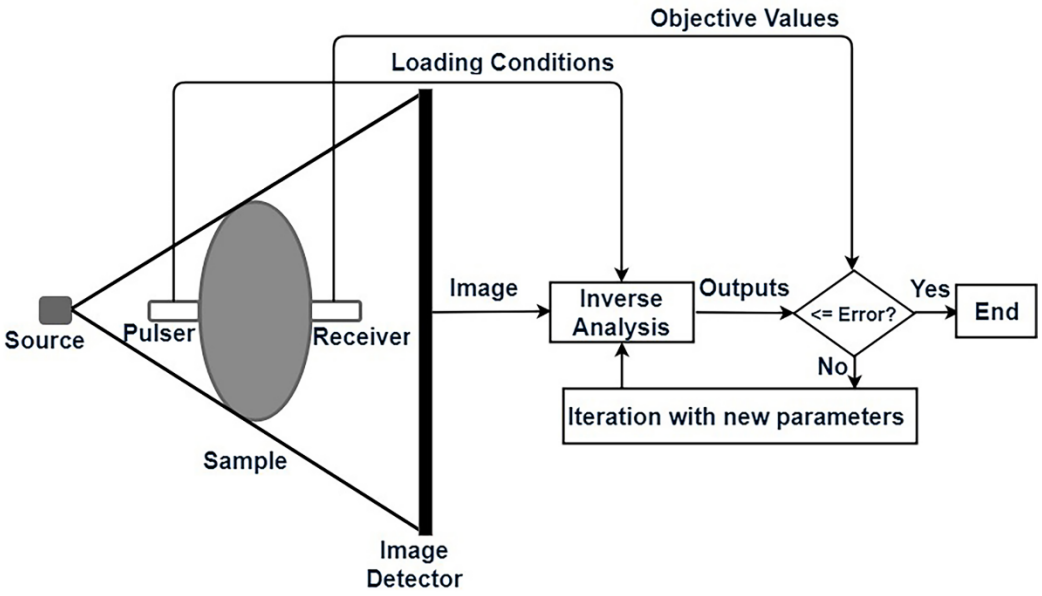

Fig. 3. Elastography based on tomography image and sound wave integration. The pulser and receiver are the sound-wave transducers. The cycle starts with image acquisition on the sample and ends up with the match between the computational output and the objective value collected by the receiver.

Inversely mapping elastography is an optimization problem to find a set of variables making the objective function maximum or minimum. However, it is difficult to establish an explicit relationship between the transmitted signal and the elastic modulus. In physics, they are interrelated. In the study, the factorial design including the full factorial design and the orthogonal array design are employed to perform the inverse analysis [107], [108]. The design assembles all or part of possible combinations of optimization variables into an array of which the optimum values will be selected out, especially suitable for problems without explicit relationships between the objective value and corresponding optimization variables. Factorial design allows evaluating all variables' effect on the objective value in a single experiment (simulation). Currently, the variable and the objective function are bridged in the FEM simulations, following the factorial design. Based on the results of all simulations, the optimum values can be found. The full factorial design needs at least two

factors (namely optimization variables), assigns possible values (also called levels) for each factor and, thereafter, executes calculations on all possible combinations of all levels across all factors. After those calculations are finished, the favorable levels can be optimized out by comparing with the objective value. If the number of calculations is so huge that the computation time is unacceptable, the orthogonal array design is another choice that doesn't need to exhaust every possibility across all factors and their levels, only considering selected possible combinations listed in an orthogonal array. These combinations of an orthogonal array are not assigned randomly, but following a strict rule so they can represent and cover all ones of every possibility [108]. It is noted that the value range (the upper and lower limits) of each factor needs to be preset, and otherwise the array cannot be designed for the factorial design. Fortunately, the reasonable elastic modulus ranges for most of biomaterials and tissues are predictive throughout the published literation and books.

2.3 Numerical Validation

In this part, the integrated method is firstly demonstrated on a brain slice. The slice is an approximately 1-mm-thick corona and cut off from a cadaver as photographed in Fig. 4 (a) [109]. The photograph is formatted to TIFF files and imported into Simpleware ScanIP (Synopsys, Inc.) for segmentation. With the pixel intensity-based segmentation, the interfaces among different functional tissues are identified. It is then transformed into two-dimensional FEM meshes with four regions. Following the names and positions of tissues [109], the four regions are the cortex (C), corona radiata (CR), corpus callosum (CC) and basal ganglia (BG) as shown in Fig. 4 (b). Brain ventricles are currently treated as CC.

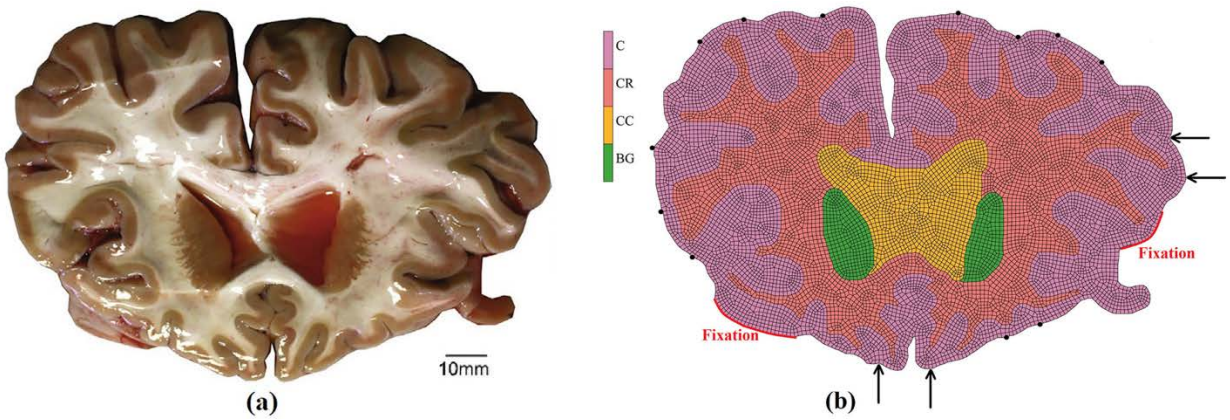

Fig. 4. (a) The brain-tissue slice photograph and (b) the four regions meshed for FEM simulation, including the cortex (C), corona radiata (CR), corpus callosum (CC) and basal ganglia (BG). The four arrows show the incidence positions and the 12 black solid dots show the signal detection locations. The 'Fixation' boundaries marked by red curves mean that displacement is constrained to be zero during FEM simulation.

Numerical model creation and simulation are conducted on the commercial FEM package, Marc Mentat 2018.0.0 (MSC Software Corporation), with the assist of a Python script performing the factorial design, the parameter update and mathematical process. The model is meshed into 11261 four-node quadrilateral elements. The incident wave is the 50 Hz sine signal applied at four positions on the outer boundary denoted by arrows in Fig. 4 (b). As denoted by the black sold dots in Fig. 4 (b), twelve locations are chosen to detect the transmission with the sampling rate of 400/s. The acquisition duration is 0.2 s. All tissues in this study are treated as linear elasticity for demonstrating the integrated method first on linear materials. The set of shear moduli, [C=1.43, CR=0.66, CC=0.35, BG=0.70] kPa, reported by Budday et al. (2017) is used as the objective values and the corresponding output at 12 locations as the objective signals. Accordingly, the eleastic moduli are [4.26, 1.97, 1.04, 2.09] kPa if Poisson's ratio of 0.49 is assumed for all tissues. The density is assumed 1000 kg/m3. In this case, full factorial design is employed to

recognize the optimality for all levels of factors. So, there are four factors corresponding to elastic moduli of C, CR, CC and BG. In terms of the reasonable ranges of their moduli, 3.0 kPa ~ 6.0 kPa for region C and 0.1 kPa ~ 3.0 kPa for other three regions, each factor is assigned eight levels at first, [3.0, 3.4, 3.8, 4.2, 4.6, 5.0, 5.4, 6.0] kPa for C and [0.1, 0.5, 0.9, 1.3, 1.7, 2.1, 2.5, 3.0] for others. Totally, it is 84 (4096) trials for possible combinations of all levels. Running on a PC with Intel(R) Core (TM) i7-3770 CPU @ 3.40GHz and 16.0 GB RAM, each trial takes 21 seconds. From this point of view, the computation of current inverse analysis is acceptable and effective. Because cross-correlation can be used to observe the similarity of two signals [110], the objective function will be established based on the cross-correlation of the objective signals and each trial ones. The maximum of cross-correlation is at the zero-lag time if two signals are identical, which is so-called auto-correlation. For this case, the objective function of the optimization problem is defined as

$$\begin{aligned} &\min f(\boldsymbol{E}) = \sqrt{\sum_{i=1}^{12}\left(1-\frac{D_C^i|_{t=0}}{D_A^i|_{t=0}}\right)^2} \\ &Subject\ to: \min f(\boldsymbol{E}) \le 1.0\% \end{aligned} \tag{3}$$

where $\boldsymbol{E} = (E_C, E_{CR}, E_{CC}, E_{BG})$, standing for the elastic moduli attempt in each level, $D_A^i|_{t=0}$ is the auto-correlation of the measured signals of point i at the zero lag time, and $D_C^i|_{t=0}$ is the cross-correlation of the trial signals and the measured signals of point i at the zero lag time. The effect of $\boldsymbol{E}$ on $D_C^i|_{t=0}$ is implicit in Eq. (3). But they are bridged in FEM in which $\boldsymbol{E}$ are the material parameter input and $D_C^i|_{t=0}$ is determined according to FEM output. The measured signals that are the objective signals come from the FEM simulation with the objective elastic moduli of [4.26, 1.97, 1.04, 2.09] kPa. Applying (3) to 4096 trials, $min\ f(\boldsymbol{E})$ is reached at [4.2, 2.1, 0.9, 2.1] kPa of the 2732nd trial, meaning that the 2732nd one is the

closest to real values among all trials. However, the error of the trial is 4.3%, larger than 1.0%. In practice, 4.3% could be enough for mapping elasticity. As an illustration for three surface locations, the objective signals of the displacement amplitude and the corresponding simulation signals of the best trial 2732 are plotted in Fig. 5 (a). By contrast, there is discrepancy for some locations between two set of signals, which causes the 4.3% error. For presenting the more accurate solution, the inverse analysis is continued until meeting $min\ f(\boldsymbol{E}) \leq 1.0\%$.

The first-round design helps to compress the value ranges for the further design. As a result, based on each value in [4.2, 2.1, 0.9, 2.1] kPa of the first-round, next round factorial design, with the smaller step, sets [3.90, 4.05, 4.20, 4.35, 4.50] for C, [1.80, 1.95, 2.10, 2.25, 2.40] for CR, [0.60, 0.75, 0.90, 1.05, 1.20] for CC and [1.80, 1.95, 2.10, 2.25, 2.40] for BG, which introduces 625 trials. This round ends up with [4.20, 2.10, 1.05, 2.10]. Because the result is almost same as that of the first-round, the step of levels is needed to be furtherly decreased. Levels of the third round are set to [4.10, 4.15, 4.20, 4.25, 4.30] for C, [2.00, 2.05, 2.10, 2.15, 2.20] for CR, [0.80, 0.85, 0.90, 0.95, 1.00] for CC and [1.85, 1.90, 1.95, 2.00, 2.05] for BG. After all trials are completed, the third round gives [4.25, 2.00, 1.00, 2.05] with 4.1%. Once more, the level range of the fourth round is narrowed down with the much smaller step, [4.23, 4.25, 4.27] for C, [1.98, 2.00, 2.02] for CR, [0.98, 1.00, 1.02] for CC and [2.03, 2.05, 2.07] for BG. Eventually, [4.27, 1.98, 1.02, 2.07] is finalized as the optimum trial with 1.0%. The comparison of the objective signals and the corresponding ones of the best trial is plotted in Fig. 5 (b) for the same locations as in Fig. 5 (a). The two set of signals are almost overlapping, which illustrates again [4.27, 1.98, 1.02, 2.07] are the optimum values, consistent with real elastic moduli of [4.26, 1.97, 1.04, 2.09] with errors 0.2%, 0.5%, 1.9%

and 1.0%, respectively. In the whole course, any internal information is not detected and processed to map the moduli. All information for the mapping is based on signals on the 12 surface locations.

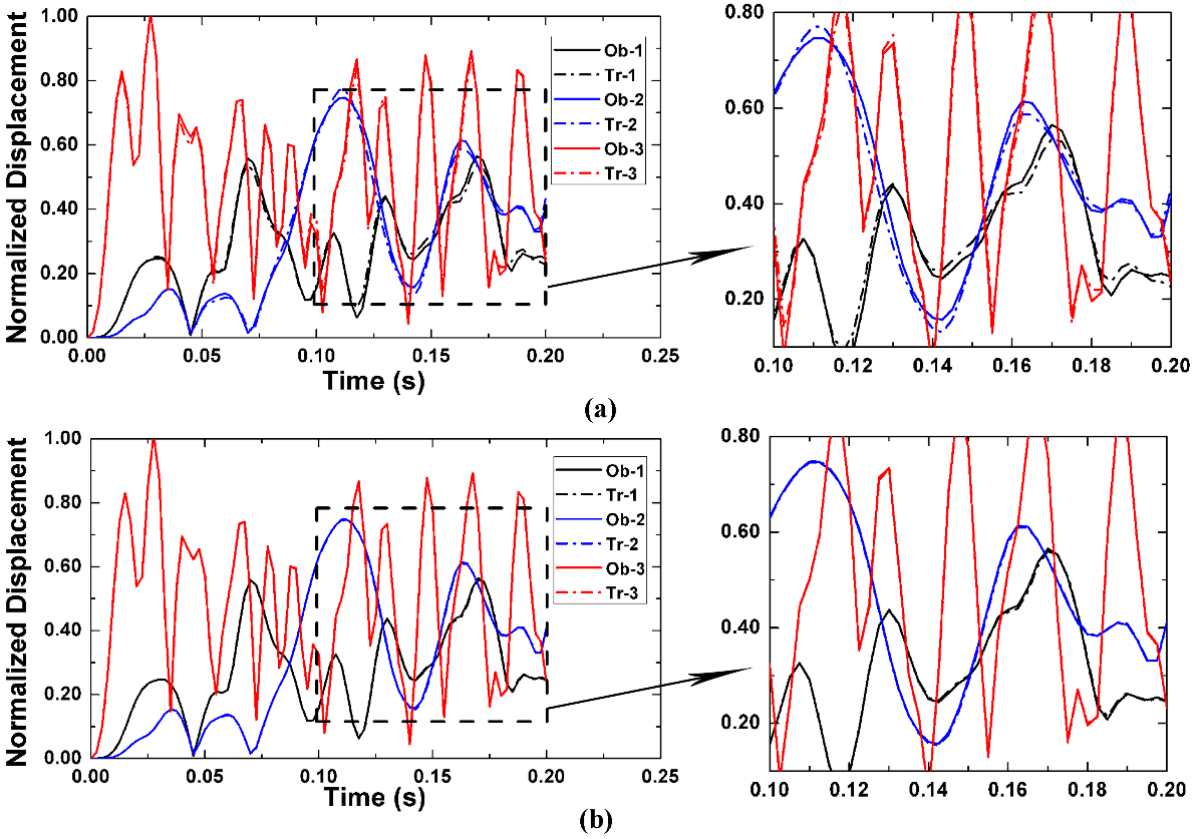

Fig. 5. (a) The comparison of the target signals and the best trial ones in the first round and (b) the comparison of the target signals and the best trial ones in the fourth round. 'Ob' stands for the target signals and 'Tr' for the output ones from the best trial.

The current study maps stiffness on segmented tomography image. For demonstrating the sensitivity to segmentation, 1.3% of CR assumed as the segmentation error is artificially merged into C as shown in Fig. 6. After analysis, the merging will introduce the 4.1% error by using Eq. (3), showing that this study has the good sensitivity to segmentation. In real cases, the brain is enclosed by a skull that may make the wave transmission too weak to be caught. However, the skull is not completely closed, having

outlets such as nose, mouth, eye, ear, and neck regions. The receivers can be placed around these regions to collect transmission.

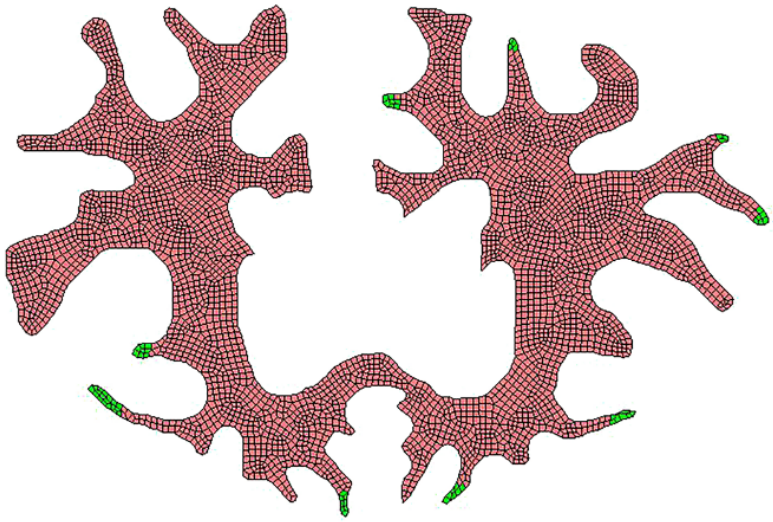

Fig. 6. 1.3% of CR, colored by green, is segmented into C and all corresponding properties are also set as same as those of C.

It is noticed that the sound incidence is compressional waves. But current study also applies to shear waves for it does not need to track and measure any internal signal, but its transmission. One of main reasons making shear wave elastography the most popular method is that speeds of compressional waves are so high that they are difficult to be tracked [33]. For the current study, there are no frequency limits because it does not need to adjust frequencies to make the wavelength measurable and trackable. However, specific frequency should be selected to make sure that the transmitted signals can be detected. For example, if the incident wave is changed to 100 Hz, following the same process of the 50 Hz analysis, it still ends at [4.27, 1.98, 1.02, 2.07] with 0.7% error. In order to basically understand the effect of signal-to-noise ratio (SNR), the measured signals that are the output under the real set of moduli are added artificially with white Gaussian noise. Fig. 7 shows a typical output of one location without noise and its corresponding signals with 55

dB SNR. Different SNR values are tried and analyzed from 50 dB to 110 dB. With the SNR increase, the error decreases quickly and approaches 0.7% as shown in Fig. 8. It can be seen that the SNR be at least up to 55 dB for having a reasonable estimation. Therefore, in practice, frequency needs to be chosen for having an enough SNR. Furthermore, the 1.0% error in Eq. (3) could be too strict because of noise in reality. For this case, if the noise level is at the SNR of 60 dB, the error is about 5%.

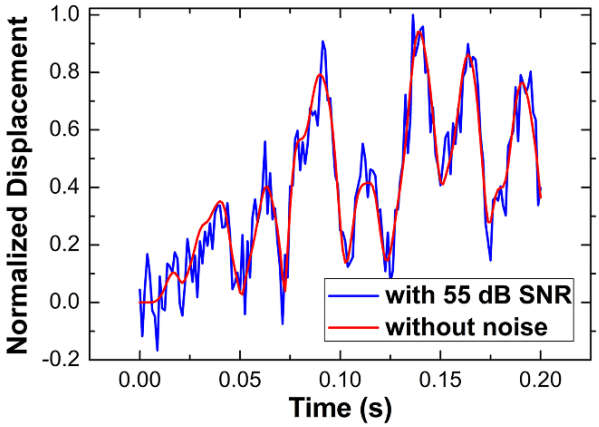

Fig. 7. A typical output of the 100 Hz sine incidence: without noise and with noise.

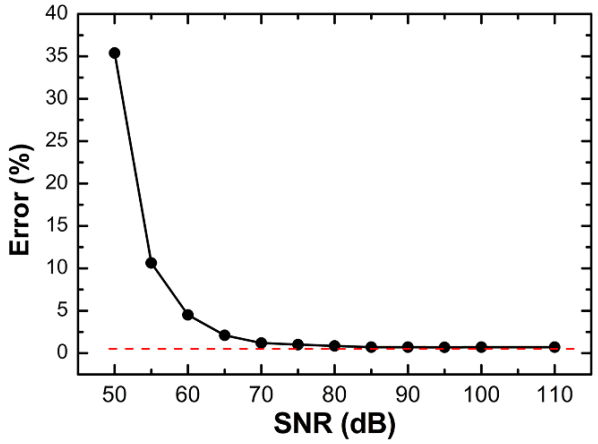

Fig. 8. Errors with different SNR values and the dash line showing the 0.7% position.

2.4 Experimental Validation

The phantom consists of the silicone rubber being the matrix and a piece of vinyl polymer being the inclusion. There are five procedures in manufacturing the phantom. First, the required amount of silicone base is poured into a plastic beaker. Second, the curing agent is added. Third, the components are thoroughly mixed by a *Caframo*™ mechanical stirrer for 20 minutes at a rotation speed of 280 rpm. The viscous media is further degassed in a vacuum for 30 minutes in order to eliminate the air bubbles trapped in the mixture. Finally, as soon as no air bubbles puff from the top surface, the polymer inclusion is dropped in. The sample in shape of the conical frustum is made after curing at room temperature for 6 days as shown in Fig. 9.

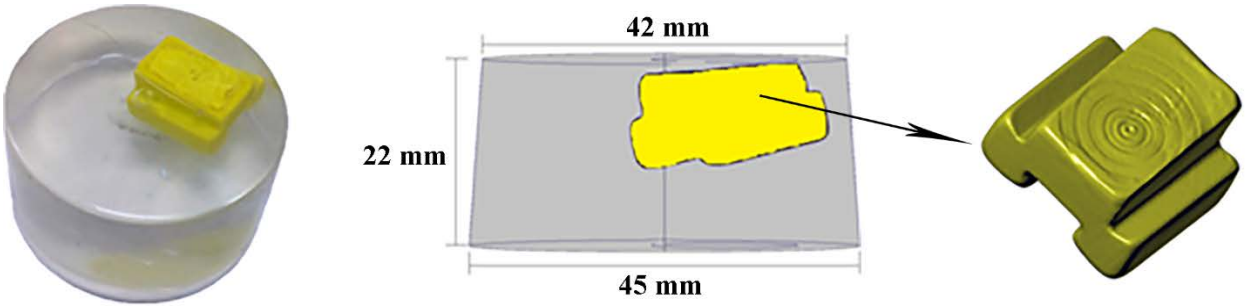

Fig. 9. Left: the phantom of silicone matrix and polymeric inclusion, Middle: main dimensions, and right: 3D inclusion image resolved by X-ray CT.

The achievement of the integrated method resides in the sample spatial structure, sound-wave test, FEM modeling and inverse analysis as stated in Section II. Because of irregularity of the inclusion geometry, its 3D image is imaged by an X-ray CT scanner, *Xradia 410 Versa* (Carl Zeiss X-ray Microscopy, Inc.) as shown in Fig. 9. The 0.4X lens with the voxel size of 25 micrometers is used to scan the inclusion. With the sample rotation step of 0.225^{o}, 1600 projections are acquired to reconstruct the 3D image. After scanning, the commercial image process software, *Simpleware ScanIP* (Synopsys, Inc.), steps into

segment based on each pixel intensity and convert X-ray CT image to a compatible format that can be imported into *Marc Mentat.*

Next is to have the soundwave tested on the sample to acquire the transmitted signals. The sound testing system is two *R3*α transducers and one *FieldCal AE Signal Generator* (MISTRAS Group, Inc.). The operation frequency range of R3α is 25 kHz ~ 70 kHz. One of transducers functions as the pulser while another one as the receiver. In the test, the incident wave is a 30 kHz sine tone burst with the peak value of 4467 Pa and 1 ms duration which is emitted by the Generator. A silicon-based lubricant is coated on sample areas on which transducers are placed. Two transducers are positioned coaxially, making waves passing through both matrix and inclusion, as shown in Fig. 10. During the test, the transmitted peak acquired by the receiver is 22.4 Pa that will be used later as the objective value of the inverse analysis. The third step is to build the computational model with *Marc Mentat*. The inclusion image scanned by Nano CT is imported into *Marc Mentat*. Because the matrix is regular, it is drawn directly by *Marc Mentat*. Both matrix and inclusion are treated as elastic materials. The loading condition is set on the position in which the incident wave is emitted by the *R3*α transducer. The whole 3D model is meshed into 89585 four-node tetrahedral elements. During the simulation, a point on the intersection of the bigger top surface and the side surface is fixed as the displacement boundary during FEM simulation.

In fact, there should be wave reflection at interface between the sample and the lubricant due to impedance mismatch. Wave undergoes two times reflection before it passes through the sample. One is on the incident interface and another on the emergent interface. The final transmission is affected by the two reflection and has a connection with

the signal amplitude and material properties. At this point, FEM simulation needs to take reflection into account as following,

$$P_t = TP_0 \tag{4}$$

$$T = \frac{2Z_2}{Z_1+Z_2} \tag{5}$$

where P_0 is the incident pressure emitted directly from the transducer, P_t is the transmitted pressure, T is the transmission coefficient defined as the fraction of the incident pressure, Z is the acoustic impedance that is the product of density and sound wave speed, and the subscripts 1 and 2 represent media proximal and distal to the interface [111].

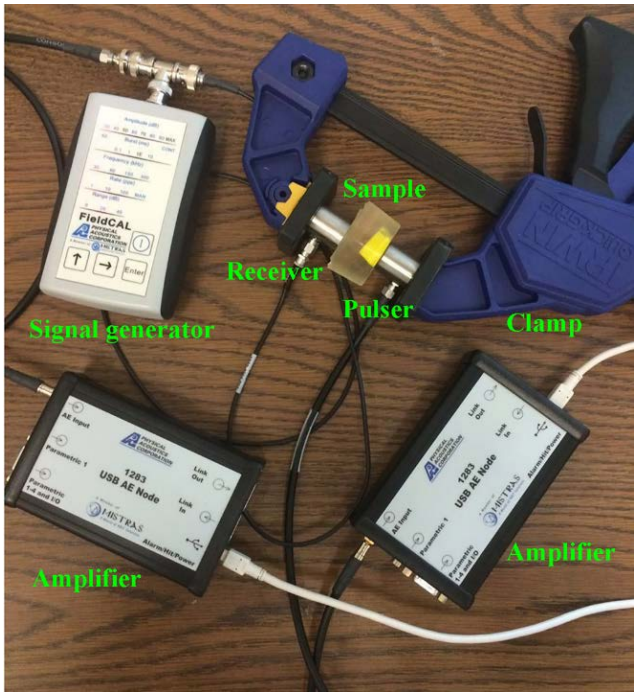

Fig. 10. Sound test on the sample. One transducer serves as the pulser and the other serves as the receiver. The incidence of a 30 kHz sine tone burst is generated by the signal generator.

The last step is to conduct inverse analysis. In the case, six factors are designed: moduli, Poisson's ratio and density of both matrix and inclusion. If five levels are associated

with each factor, the full factorial design needs totally 5^6 (15625) trials, which is time-consuming in computation. In order to reduce the number of trials, an orthogonal array is specifically designed to investigate this inverse analysis. As for the six 5-level factors, there are 25 trials according to the principle of the orthogonal array design [108]. Mathematically, the 25 trials can represent 15625 ones of the full factorial design. It must be kept in mind that the transmission coefficient of every trial should be updated with (5). The amplitude of incident wave into the sample keeps updating with (4) as well for each trial during FEM simulating. In the 3D simulation, each trial takes 4 minutes, meaning 100 minutes for total 25 trials. From this point of view, the computation of current inverse analysis is acceptable and effective. Likewise, the orthogonal design needs the possible range of each factor value that will be narrowed down since the initial rough estimation. The finalized levels of each factor are listed in Table 2. In the column 'Factors', 1, 2 and 3 denote the modulus, the Poisson's and the density of matrix, respectively, and 4, 5 and 6 denote the modulus, the Poisson's and the density of inclusion, respectively. After the 25 trials are finished, the difference between the peak pressure of FEM output and the experimental peak (22.4 Pa) is calculated for each trial. Then, the difference is classified by levels for each factor and averaged over the number of levels as shown in Fig. 11 from which the optimum levels corresponding to the minimum average can be read out directly: modulus of 2.0 MPa, Poisson's ratio of 0.30 and density of 1050~1150 kg/m^3 for matrix, and 2.6 MPa, 0.39 and 1600~1700 kg/m^3 for inclusion. The density is given in a range, illustrating that the objective value is not sensitive to density variation in contrast with other factors. Fig. 12 shows the computational output of the optimum levels which gives

the peak of 21.5 Pa, matching well with the measured value of 22.4 Pa with the 4.0% error. With numerical errors and measurement noises, 4.0% may be considered good match.

Table 2. Levels for six factors

Factors	Levels				
	1	2	3	4	5
1	1.2	1.6	2.0	2.4	2.8
2	0.30	0.35	0.40	0.45	0.49
3	1000	1050	1100	1150	1200
4	2.2	2.6	3.0	3.4	3.8
5	0.35	0.39	0.43	0.47	0.49
6	1500	1600	1700	1800	1900

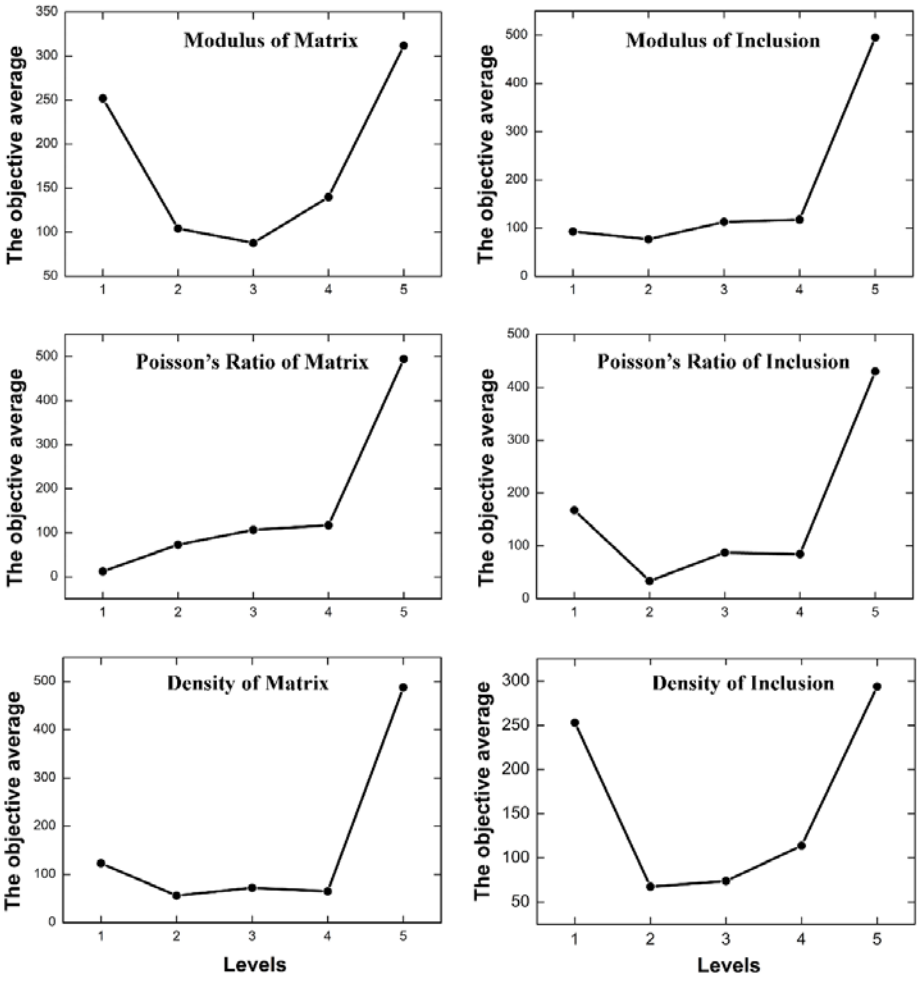

Fig. 11. The FEM output average of each level of every factor: x-coordinate is the level number for each factor, and y-coordinate is the output average corresponding to each level. The level holding the minimum average is optimum.

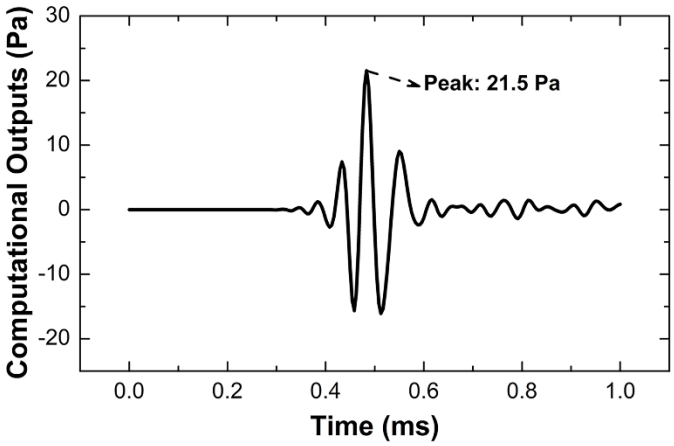

Fig. 12. The FEM pressure output with optimum values: modulus of 2.0 MPa, Poisson's ratio of 0.30 and density of 1050 kg/m^3 for matrix, and 2.6 MPa, 0.39 and 1600 kg/m^3 for inclusion.

Although the integrated method has completely been applied to the phantom and those unknown properties obtained, there still is a doubt whether those optimum values are real. For further verifying the method and the optimization, some of properties are measured experimentally. The density and moduli of matrix and inclusion are measured for the verification. The mass is tested directly by a balance and the volume by a graduated cylinder and water. The volume is the difference of the two readouts of water surface positions before and after the matrix or inclusion is put in the cylinder. At last, the density of matrix is 1050 kg/m^3, and the density of inclusion is 1690 kg/m^3. Both values are all in the optimization range of density, meaning that their optimum values agree with measurements. The modulus is measured through the uniaxial compression by the tester, *BOSE ElectroForce® 3200*. The sample for matrix is a cylinder of 9.7 mm × 9.6 mm, and the sample for the polymer inclusion is a cuboid of 11 mm × 9.4 mm × 5.7 mm. The compression speed is 0.01 mm/s under the displacement control. Five tests are conducted for each sample, and then followed by the linear fit on stress-strain curves as shown in Fig.

13. The slopes are the moduli: 2.1 MPa for matrix and 2.6 MPa for inclusion. By comparison, the optimum values of 2.0 MPa and 2.6 MPa are consistent with the measured moduli for matrix and inclusion, respectively.

Overall, as demonstrated on the 2D case and the 3D phantom, the integration method can predict the accurate elasticity. Because the objective value is not built as the explicit function of variables, factorial design provides a way making the inverse analysis effective and controllable. It is also noted that the current investigation is limited under the assumption of isotropic elasticity of tissues. Future work is needed to extend the method for general anisotropic elastography

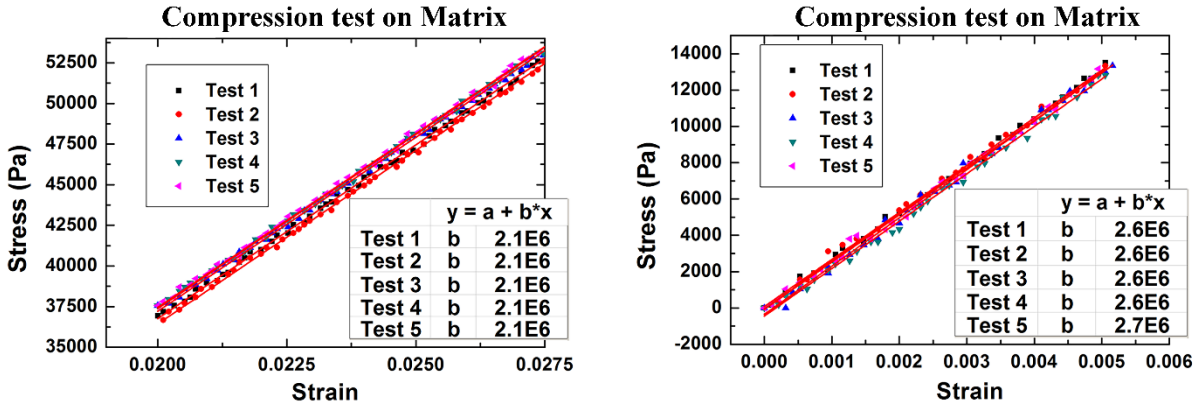

Fig. 13. Compression stress-strain curves and their linear fits: the slopes are the moduli. All of five tests on each sample show good repeats.

2.5 Conclusion

A sound transmission-based elastography method is developed, which is validated on 2D and 3D cases with different waveform input and frequencies. This method can potentially be an effective tool in both fields of charactering elasticity of biomaterials/tissues and engineering materials. While the experimental validation of the method uses X-ray tomography image, other imaging modalities may work as long as they

can provide the geometric delineation. One of the unique features of the current study is that no interior responses within objects, such as displacement, strain, or wave speed, need to be measured in advance for mapping elastography. At this standpoint, samples act as a "black-box" which also makes the experimental measurement free of considering the reflection and the refraction inside the object. Another feature is that the tomography image containing the geometric structures and sound wave carrying the material properties are integrated into FEM in which sound wave test is simulated and analyzed inversely to map the mechanical properties. Fundamentally, the current method is free of the frequency effect because it doesn't need to adjust the frequency to make internal responses trackable and measurable. Simulations and phantom experiments have been conducted to validate the proposed integrated method. The optimum results of density and moduli have been verified with the experimental measurements.

Chapter 3 Deep Learning Driven Elastography

3.1 Introduction

As discussed in Chapter 2, the factorial design was used in inverse analysis. Although the first round had contained enough information for narrowing down to next round, the whole factorial design process had to be went through for every single round. If the elastography could be mapped only by the first round, that would be more attractive and efficient. Machine learning (ML) will be the first choice because it is a powerful tool in data process. Some efforts of ML have been put in elastography [112]–[114]. But they mainly focus on image enhancement and are not suitable for processing the signals such as the transmission data raised in Chapter 2. The advent of machine learning, especially convolutional neural networks (CNNs) in deep learning, accelerates and improves the process of large data [113]–[117]. It is well known that deep CNNs have gained huge achievements in image classification and process. The deep CNN, being a kind of feature-extraction-based machine learning networks [118], [119], has potentials for regression analysis [119]–[122]. CNNs execute regression with less physical process and allow multi-output, relying on convolutional filters and corresponding trainable weights.

In this Chapter, a deep CNN architecture is proposed and investigated to map the elastography based on transmissions of wave. The architecture, while built up based on the traditional sequential structure, considers the passing efficiency of parameter gradients and the features of raw data. Its prediction and accuracy are validated with the first round of factorial design of the brain slice described in Chapter 2, and then, with a 3D model built directly from a brain MRI image. In addition, as an investigation extension of the developed

CNN architecture, its capability of structural health monitoring is also demonstrated under condition of the coexistence of a bore crack and a delamination in the propellant grain of solid rocket motors (SRMs).

3.2 Deep CNN Architecture

Considering the passing efficiency of parameter gradients and the contribution of raw data, the deep CNN architecture proposed in the study is shown in Fig. 5 on which names starting with “conv” stand for convolutional layers, with “relu” for rectified linear unit layers and with “mp” for maximum pooling layers. Regarding others, “datainput” means the input layer, “add_1” the addition layer which sums the outputs from previous layers, “concat_1” the concatenation layer which concatenates the outputs from previous layers, “ap_1” the average pooling layer, “fc” the fully connected layer and “regoutput” the regression output layer. MATLAB is employed to establish networks and perform training. In the architecture, there are four convolutional layers, three of which form the main branch and sequentially connect each other. The fourth one forms the sub-branch and connects with the input directly and meets with the main branch at the addition layer, which makes the parameter gradients passing more efficient. Any defect is expected to affect the radial stress field. For having the contribution of raw data to the feature extraction, the second sub-branch has no convolutional layers between the input and output. If the second sub-branch is directly connected to the addition layer, more convolutional layers may be added in for matching down with the input data dimensions. As a result, the computation time not only will be increased, but the accuracy be affected due to less kernels at the end. In this study, the trade-off is solved by concatenating input

data with the output of the addition layer as shown in Fig. 14. In other words, the input data are simply appended to the convolved data channels at the concatenation layer, which makes the current architecture different from the inception module [123].

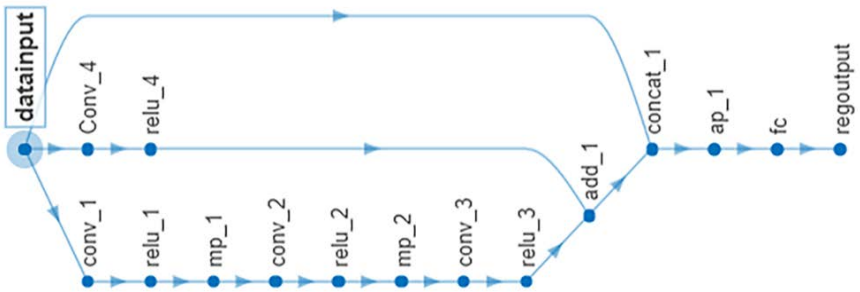

Fig. 14. Deep CNN architecture for mapping elastography.

3.3 Validation

The same padding is used for convolutional layers and pooling layers. The stride is set 1 for all corresponding layers. The optimizer is Adam that is a method for stochastic optimization [124]. The loss function is mean-squared-error for the regression layer that outputs crack lengths and delamination angles. While both conv_1 and conv_2 have 64 kernels with the size of 1×8, conv_3 and conv_4 each have 32 kernels with 1×8 and 1×1, respectively. All pooling layers have the same size, 1×4. If each dataset is organized as the 12-channel structure accommodating signals of 12 locations, the dimensions are 1×81×12. The details of the CNN architecture are listed in Table 3.

Table 3. Details of the CNN architecture

Layer	Name	Activations	Learnables
1	datainput	1×81×12	-
2	conv_1	1×81×64	Weights: 1×8×12×64 and Bias: 1×1×64
3	relu_1	1×81×64	-
4	mp_1	1×81×64	-

5	conv_2	1×81×64	Weights: 1×8×64×64 and Bias: 1×1×64
6	relu_2	1×81×32	-
7	mp_2	1×81×32	-
8	conv_3	1×81×32	Weights: 1×8×64×32 and Bias: 1×1×32
9	relu_3	1×81×32	-
10	conv_4	1×81×32	Weights: 1×1×12×32 and Bias: 1×1×32
11	relu_4	1×81×32	-
12	add_1	1×81×32	-
13	concat_1	1×81×36	-
14	ap_1	1×81×36	-
15	fc	1×1×4	Weights: 2×2592 and Bias: 4×1
16	regoutput	-	-

Known from Chapter 2, the first round of the brain slice contains 4096 datasets labelled with corresponding modulus values of four regions as shown in Fig. 4. 400 out of 4096 datasets are used for validation in the process of training and others for training. Therefore, the training input is the 4D matrix of $1 \times 81 \times 12 \times 3696$. The training parameters, also called hyperparameters, are set 0.001 for the initial learning rate, 64 for the minibatch and 50 for the maximum epochs. Finally, the training takes 11 minutes running 2850 iterations on a single Intel® Core™ i7-3770 CPU with 64-bit operation system and ends at the root-mean-squared-errors (RMSEs) of 0.25 kPa. If the objective displacement of the 12 locations are fed into the trained network of Fig. 14, the predicted moduli are 4.1695, 1.9724, 1.0523 and 2.1135 for C, CR, CC and BG, respectively. Compared with the real values of 4.26, 1.97, 1.04 and 2.09, the errors are -2.1%, 0.1%, 1.2%, 1.1%, respectively. It is concluded that CNNs can accurately map elastography. Furthermore, deep learning is more powerful to extract the useful information than the multiple factorial design. But the factorial design is a good start for providing the training data.

For furtherly validating the proposed deep learning architecture, a 3D model is meshed based a brain MRI image as shown in Fig. 15. The model consists of 5 materials, skull, scalp, white matter (wm), grey matter (gm) and meninges, and contains 54833

hexahedral elements of eight-node. The element size is 4 mm. The stimulus of 500 Hz sine is applied to the region inside mouth as denoted by arrows in Fig. 15. The time step is 0.25 ms in 0.03 s duration. Because the skull is much stiffer than other materials and well known with modulus, its modulus is not treated as a variable, but a constant during the forward simulation. Therefore, there will be four unknown materials, i.e., scalp, wm, gm and meninges.

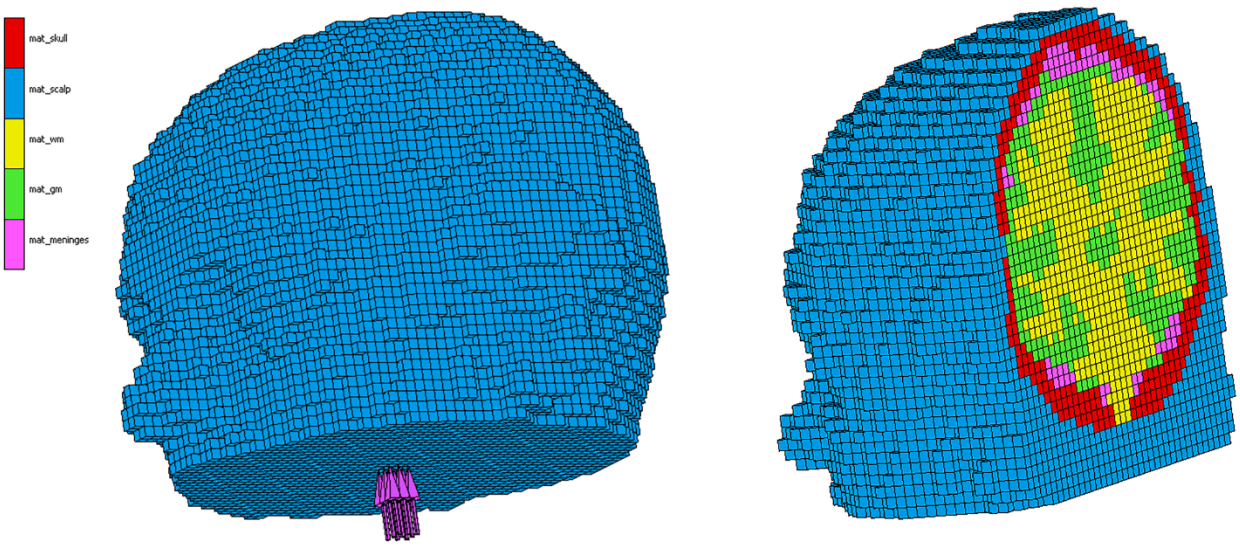

Fig. 15. Mesh of 3D head model

The real values of all moduli are set with 6500 MPa, 16.7 MPa, 0.12 MPa, 0.075 MPa and 31.5 MPa, respectively. Again, the full factorial design is used to generate training data. Seven levels, [10, 15, 20, 25, 30, 35, 40] MPa, are assigned to scalp and meninges, [0.02, 0.04, 0.06, 0.08, 0.1, 0.12, 0.14] MPa to wm and gm, which will give 2401 datasets. Signals at 14 locations in regions of eyes and ears (3 locations at each eye and 4 at each ear) are acquired which are expected without going through the skull, which can be illustrated by Fig. 16. Obviously, the signals out of regions of eyes and ears are stronger than those through skull. 200 datasets out of 2401 randomly picked out for validation in the training

process. In the training of the 3D model compared with the 2D one in Table 3, the input is 1×121×14, the learning is 0.0001 and all kernel sizes are doubled. Because the moduli of wm and gm are too small to excel numerical errors and converge to an accurate prediction, their corresponding labels are multiplied by 300. Finally, the deep CNNs deliver the predictions of scalp, wm, gm and meninges with errors of 3.1%, 3.0%, 5.0% and 8.8%, respectively. If the labels of wm and gm were not amplified, the errors were 3.0%, 16.7%, 6.7% and -22.2%.

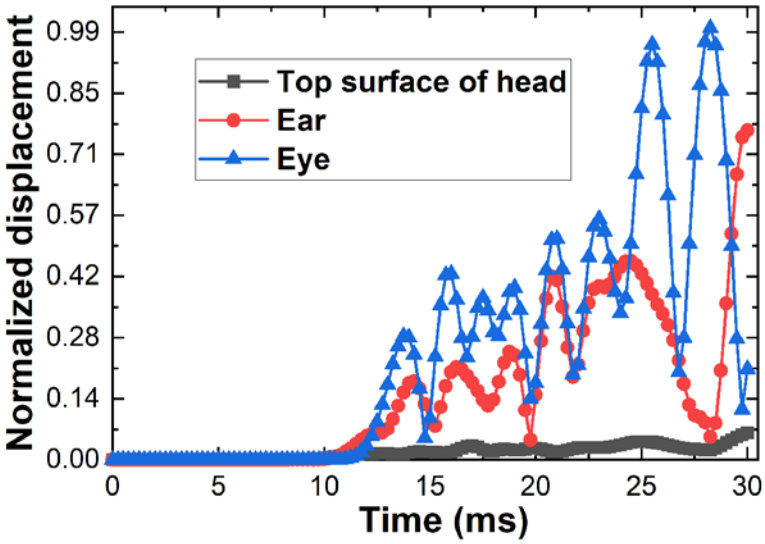

Fig. 16. Comparison of signals out of eye, ear and skull

3.4 Extended Investigation

3.4.1 Introduction

Since solid rocket motors (SRMs) are used in applications such as commercial launch vehicles and defense missiles, their durability and reliability draws much attention [125]–[129]. One of the major concerns is the structural integrity of propellant that is directly associated with functioning of SRMs. The two major defects, inner bore cracking and propellant delamination with the insulation layer, are critical to the structural integrity

[126], [130], [131]. Bore cracking can cause burn-surface abnormalities and delaminations may cause case burn-through [128], [129], [132]. The temperature changes that the motor experiences during its lifetime have been acknowledged as the main reason leading to cracks and/or delaminations. These temperature changes cause stress concentrations at the inner bore and at the interface between the propellant and the insulation [130]–[132]. In manufacturing, the propellant cures at temperatures slightly above the room temperature (RT) and cools down to RT. In the process, crack and delamination may occur or be initiated. Thereafter, especially for tactical rockets, more extreme temperature variations are expected in storage or service, which may further initiate new defects and/or propagate existing ones. For the sake of detecting the mechanical responses inside propellant during thermal cycling, sensor technologies have emerged to monitor stress or strain evolution [130], [132]–[138]. One of the important efforts is to estimate the defect inversely based on the measured signals, so that the structural integrity can be judged [126], [129], [132]. Current methods are still on tracking and analyzing mechanical response for finding explicit relationships, only focusing on a single defect that is either crack or delamination [126], [129]. On the other hand, the prediction accuracy depends on the number of sensors and the sensor positions [129], [131]. Although more sensors help to more accurately detect and estimate defects, they are also possible failure sources and make the manufacturing process more complicated. Furthermore, from the physical point of view, since the relationships between measured signals and the defect sizes are hard to establish explicitly, direct curve fitting methods by regression become cumbersome. Although machine learning has been related to rockets [139], [140], much more research

needs to take place. With the development of sensor technologies, it is deemed that machine learning will power data fusion [141].

In the extended investigation, with a focus on the coexistence of a bore crack and a delamination in propellant of SRMs, the training data are derived from numerical simulation of FEM and fed into the network of Fig. 14 for predicting defect sizes. The input data structures with one channel and multi-channels are discussed and compared in context.

3.4.2 FEM Simulation

For being triggered to predict defect scales, CNNs need to be trained with labeled data first. Then, unlabeled data can be fed in and identified. FEM has been implemented to investigate structural responses with defects in SRMs [126], [129], [142], [143]. In this study, considering the propellant based SRMs as a 2D structure, FEM simulation is used to generate input data tagged with labels. As shown in Fig. 17, the propellant structure is axisymmetric with the insulation and the case attached outside. The inner and outer diameters of the propellant are 203.2 and 406.4 mm, respectively. The thicknesses of the insulation and the case are 2.54 mm and 3.175 mm, respectively [126]. All materials are treated as elastic, with the propellant (grain) and insulation dependent on temperature as shown in Fig. 18. Young's modulus of the case is 55900 MPa. Poisson's ratios are 0.499, 0.499 and 0.3 for propellant, insulation and case, respectively. The corresponding expansion coefficients are 9.56×10^{-5}, 8.75×10^{-5} and 2.16×10^{-6} [126].

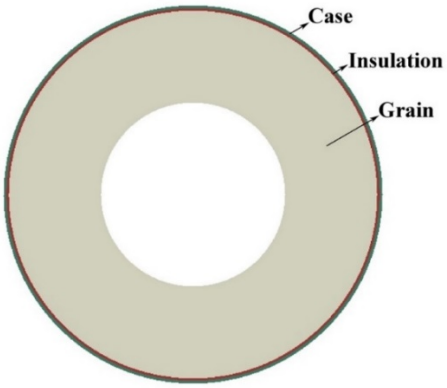

Fig. 17. Structure of propellant, insulation and case

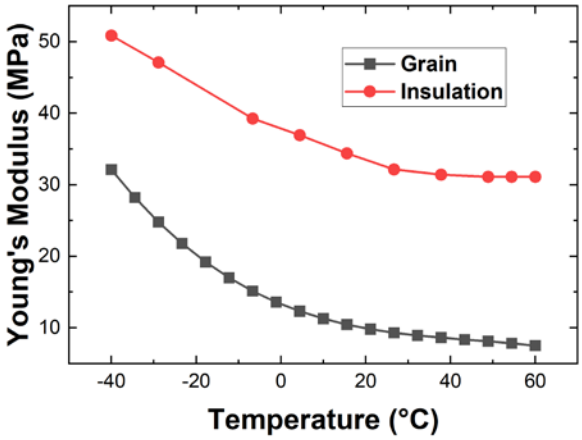

Fig. 18. Dependence of Young's modulus on temperature

All simulations are modeled and conducted by the commercial FEM package, *ABAQUS* (2018). In total, the structure is meshed into more than 6500 four-node quadrilateral elements of plane-strain in which crack tip regions, the thin case and insulation are meshed much more finely [126]. The temperature loading history is from 60 °C to - 40 °C [126]. The bottom point is fixed for all directions and the top one is fixed in the horizontal direction. The load step is -1 °C, staring from 60 °C during the simulation. Because the accuracy of the stress sensor is ~10 kPa [126], [129], small defects may not be sensed as shown in Fig. 19. Here the vertical axis is the stress difference between the defect and no-defect simulations, and the horizontal axis is the circumferential angle along the

interface of propellant and insulation. The delamination is denoted by debonding angles. It can be illustrated that 4-sensor deployment may not detect the changes of stress less than 10 kPa when the crack is less than 11 mm or the delamination less than 16°. It also can be seen that there is an apparent stress concentration around defect tips. Accordingly, the training data will be simulated and collected among combinations of eight crack lengths in [11.0, 16.1, 21.5, 26.0, 31.0, 35.9, 40.9, 45.8] (mm) and eight delamination angles in [16°, 20°, 24°, 28°, 32°, 36°, 40°, 44°]. It is known that the superposition principle applies to stress fields because of linear elasticity, which allows that a combination case of crack and delamination can be obtained through superposition of a single crack stress field and a single delamination one. For example, the combination of one 11.0 mm bore crack and one 20° delamination is simulated directly and compared with the superposition of their individual fields as shown in Fig. 20. It is noticed that the direct simulation and the superposition are overlapped, proving the superposition principle and helping to reduce the computation time for analyzing possible combinations. In other words, the simulation is only run on each of eight crack and eight delamination cases individually instead of on their combinations.

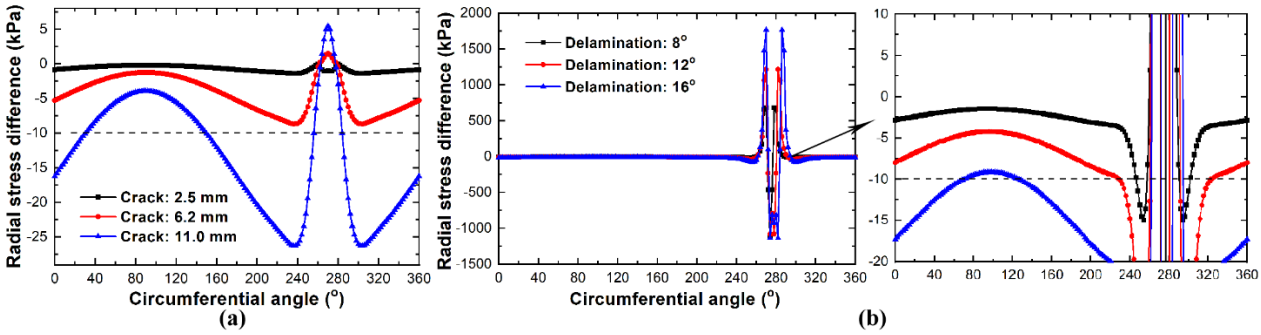

Fig. 19. Stress difference between defect and no-defect: (a) Crack and (b) delamination

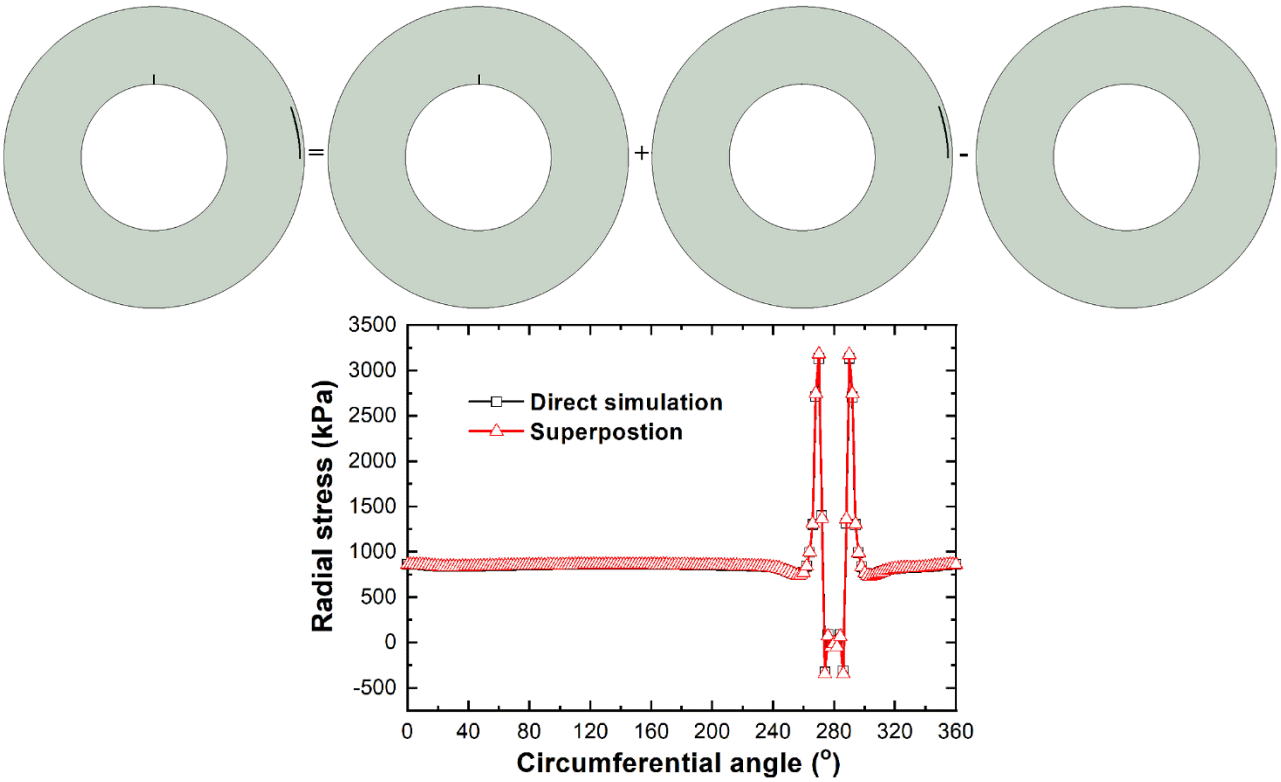

Fig. 20. Superposition of stress fields

In this study, it is assumed that there are four sensors deployed evenly along the circumferential interface between insulation and propellant. If there are not any defects, the four sensors' readings are all the same with each other. For strengthening the stress change caused by defects, the no-defect data are treated as the origin and deducted from data with defects. In terms of axisymmetry, the relative location of the sensor array and a defect can be controlled by rotating the array along the interface. As aforementioned analysis, the stress fields experienced with a coexisting crack and delamination can be realized using superposition. Eight crack lengths and eight delamination angles are considered, giving 64 possible combinations. In each of these combinations, there are 20 sub-combinations if the angular distance between the crack and the delamination is varied in 18° increments from 0° to 360°. Furthermore, each of these sub-combinations contains

18 combinations if the angular distance of the sensor array is varied in 20° increments from 0° to 360°. The total of all these possibilities (64×20×18) gives 23040 datasets, which are collected for training CNNs. These datasets are expected to be good enough for training because CNNs are a feature aimed training process, these relative distances are not expected to have apparent effects on the extraction of features. It can be understood from another point of view that, for example, a specific object can always be identified wherever it is on a picture.

3.4.3 Prediction of defect sizes

Eighty percent of the 23040 training datasets were actually used for training, with ten percent held back for validation in the process of training and the remaining ten percent being used for post-testing of the trained network. Therefore, the training input is the 4D matrix of 1 ×101 ×4 ×18432. To ensure that all values are positive, the minimum value is subtracted from its corresponding signal set. The training parameters, also called hyperparameters, are set 0.001 for the initial learning rate, 128 for the minibatch and 100 for the maximum epochs. Finally, the training takes 88 minutes when running 14400 iterations on a single Intel® Core™ i7-3770 CPU with 64-bit operation system. Out of the test data pool, 200 datasets are randomly chosen for post-test as plotted in Fig. 21, showing the trained network performance at the root-mean-squared-errors (RMSEs) of 3.2 mm for crack and 2.0° for delamination. It can be seen that the deep CNN can accurately predict crack lengths and delamination angles. If the second sub-branch is removed, the training takes 100 minutes and ends at RMSEs of 3.6 mm for crack and 2.2° for delamination. It is

proven that considering the original input further accelerates the efficiency of the useful information extraction.

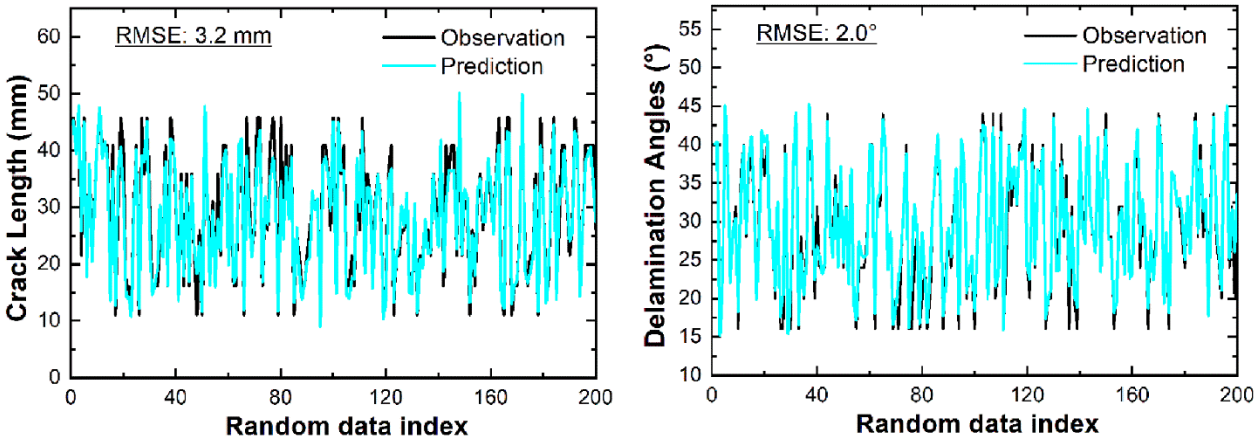

Fig. 21. Perditions of crack and delamination with the trained network

There is another input data structure available by arranging the signals of four sensors as one-channel dataset, i.e. 4 ×101 ×1 instead of 1×101×4. Although it seems like a small change and that delivers similar accuracy, the training time increases dramatically to 491 minutes due to nearly fourfold activations and learnable weights. Therefore, the 4-channel data input is recommended and used for following discussion.

For having the comparison with the architectures without any sub-branches, two sequential CNNs are established and trained with two convolutional layers and five convolutional layers, respectively, as shown in Fig. 22. While the first convolutional layers in Fig. 22 (a) and the first three convolutional layers in Fig. 22 (b) have 64 kernels, the remaining convolutional layers are assigned with 32 kernels. The settings of other layers and all strides in Fig. 22 are same as those used in the 2D brain slice, including the hyperparameters. The performance of the two sequential CNNs is plotted in Fig. 23. The accuracy comparison of different architectures is graphed in Fig. 24. It can be illustrated

that the sequential architecture with at least five convolutional layers can approach the proposed architecture in accuracy, taking a longer time of 162 minutes.

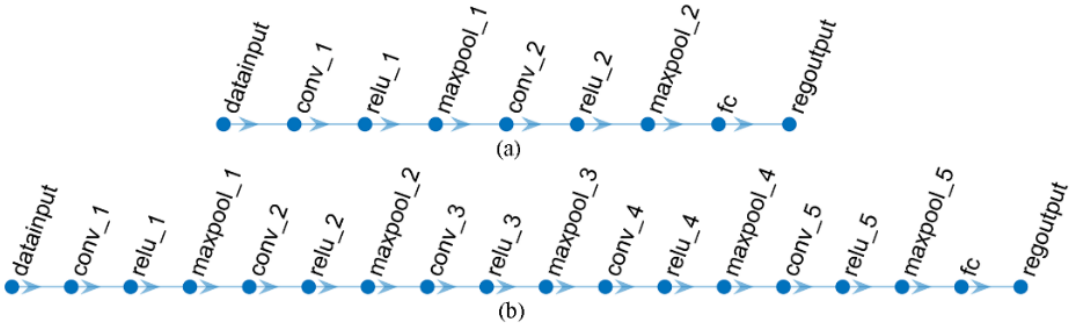

Fig. 22. Sequential CNN architectures: (a) with two convolutional layers and (b) with five convolutional layers

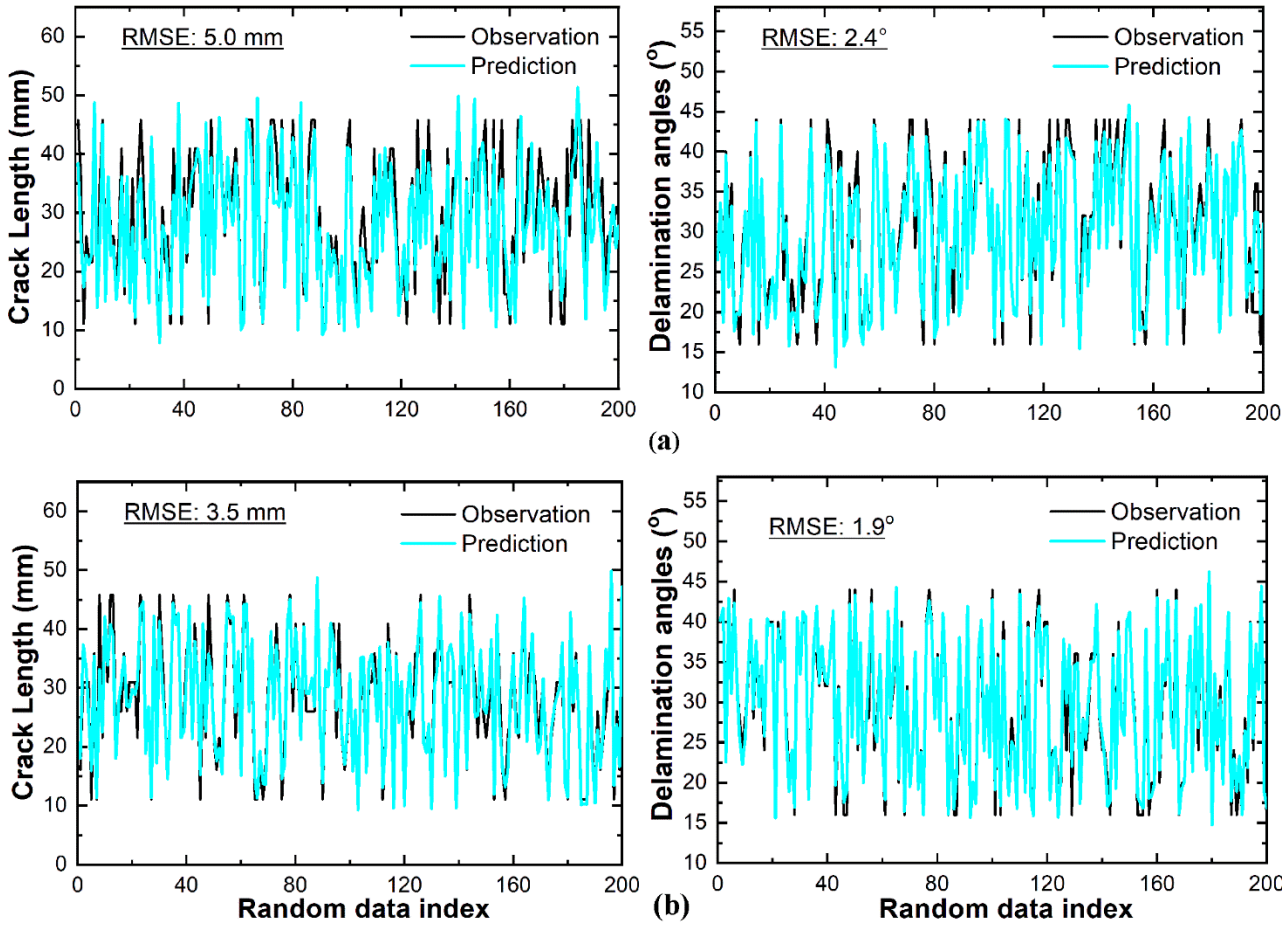

Fig. 23. Sequential CNN predictions (a) with two convolutional layers and (b) with five convolutional layers

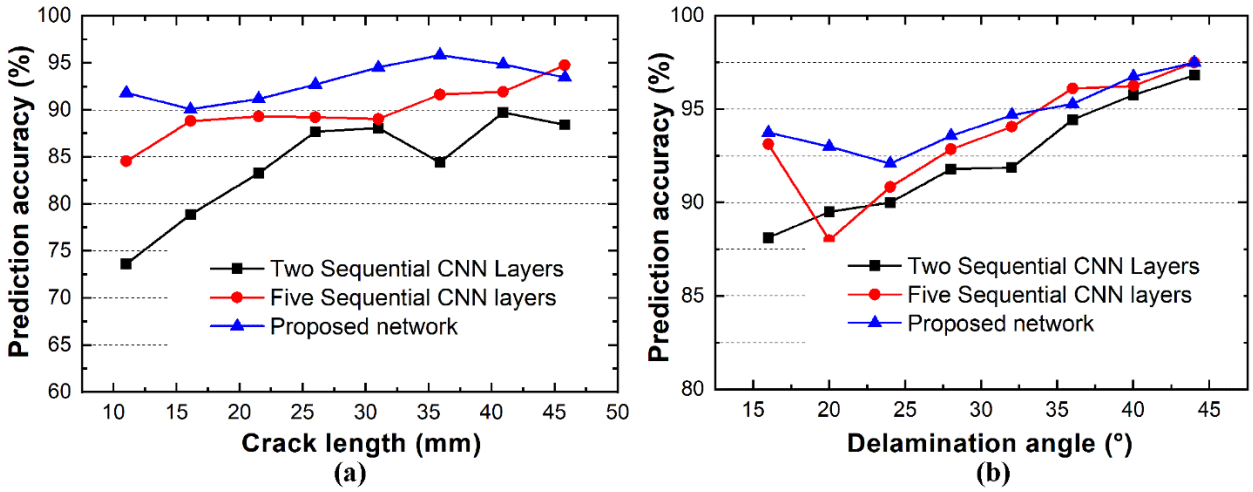

Fig. 24. Prediction accuracy of different architectures: (a) Crack and (b) delamination

Learned from these results, the bore crack quantification is the major factor affecting the convolutional layers amount, rather than the delamination magnitude. Even in the deep CNN with two convolutional layers, the delamination prediction is acceptable. Because the magnitude of crack-induced stress variations is much smaller than of delamination-induced variations as shown in Fig. 19, to extract the crack description out of the delamination dominant information requires more layers. Likewise, the number of kernels of the convolutional layer is controlled by crack signals. For example, if the first convolutional layer of the network in Fig. 22 (a) is replaced with a 32-kernel layer instead of a 64-kernel one, the crack RMSE is 7.4 mm while the delamination RMSE is 3.1°. However, it is not telling that the accuracy can be improved by more and more kernels. When the kernels are beyond 64, the improvement is very limited.

3.5 Conclusion

A deep CNN architecture is proposed for mapping elastography and quantifying the defect sizes for structural health monitoring. The architecture not only considers the passing efficiency of parameter gradients, but also takes the original information of input data into account. For validating the CNN, the first-round data of the factorial design of the brain slice is employed to generate the labeled training data. With the greater efficiency, the accuracy of the proposed the deep CNN architecture is almost equal to of the analysis of the multiple factorial design. In addition, the proposed network can be used to predict defect size in structural health monitoring and be validated through the coexistence of bore crack and delamination in the propellant structure of SRMs.

Chapter 4 Wave Deformation Untangled Elastography

4.1 Introduction

It has been recognized that pathological changes of many biological tissues correlate with their mechanical properties, commonly, the Young's modulus or shear modulus, which motivates a new modality of medical imaging, i.e. elastography mapping with stiffness distribution [9], [10], [12], [14], [18], [55], [84], [144], [145]. The stiffness variation through all tissues is over five orders of magnitude while other commonly used modalities (CT, MRI and Ultrasound) can detect variation in two orders [13]. At this standpoint, elastography is more promising in identifying abnormal tissues. To this end, the dynamic elastography prevails, reconstructed through analyzing the motion responses to external excitations generating harmonic or transient waves. The governing equations are Eq. (1). Accordingly, one more relationship can be obtained except Eq. (2),

Since the shear wave (SW) cannot change volume and the curl of displacement field of compressional wave (CW) is zero, the velocities of compressional and shear waves are deduced, respectively, through Eq. (1) as

$$V_c = \sqrt{\frac{E(1-\nu)}{\rho(1+\nu)(1-2\nu)}} \tag{6}$$

where V_c is the speed of CW, V_s is the speed of SW, ν is Poisson's ratio and E is Young's modulus equal to $2\mu(1+\nu)$ [94], [95]. Most of elastography reconstruction models focus on SW-induced responses because its speed is more trackable than that of CW in tissues [33], [94], [144]. Direct measurement is to track SW motions to measure the wavelengths or wave speeds, followed by elastographic image based on Eq. (2) [55], [58], [84], [90], [99]–[101]. Such shear-wave elastography (SWE) is realized by ultrasound and magnetic

resonance techniques, which has great potential as a clinical imaging tool for health care in recent years [146]–[154]. However, complex geometries, boundary reflection and refraction at tissue interfaces, and mode conversion may cause the direct measurement elusive, leading inaccurate detection [11,17,26–28]. To correct these influencing factors and accommodate the more common deformation scenarios of combined SW and CW, in this Chapter, a new elastography method is developed. The method is specifically proposed for elastography mapping scenarios in which whole displacement field can be measured. MRI can provide such measurement [58], [157]. Another popular stimulus for SWE is acoustic radiation force impulse (AFRI) [43], [146], [158]. Although AFRI elastography is mapped by tracking peak displacement with ultrasound modality, the current method still works if the AFRI-stimulated deformation can be measured.

For a single wave (either CW or SW) in the propagation direction, the following relationship can be obtained through Eq. (1),

$$\dot{u}_i = V u_{i,j} \tag{7}$$

where $\dot{u}_i$ is the derivative of u_i with respect to time (i.e., transient vibration velocity), $u_{i,j}$ is the transient strain and V is the wave speed. If the wave is compressional and propagates along i-direction, $V = V_c$ and $u_{i,j}$ is the non-zero normal strain equal to volumetric strain. If the wave is shear and propagates along j-direction and parallel to the i- j plane, $V = V_s$ and $u_{i,j}$ is the non-zero shear strain. Eq. (7) becomes meaningful if the vibration velocity and the strain are known for a point.

In this Chapter, we propose a method by untangling compressional motions out of the fully coupled compression-shear strain field. The primary purpose is to decompose the coupled strain tensor by coordinate transformations and analytically untangle the CW-

based strain and SW-based strain. Elastography then is mapped with Eq. (7) and Eq. (6) or Eq. (2).

4.2 Method

If a combined CW and SW passes through a point in a global system $\boldsymbol{x}$, the deformation is a tangled field, i.e.,

$$\varepsilon_{ij} = \varepsilon_{ij}^{c} + \varepsilon_{ij}^{s} \tag{8}$$

where ε_{ij} is the total strain, ε_{ij}^{c} is the strain tensor caused by CW and ε_{ij}^{s} is the strain tensor by SW. It is assumed that the CW propagates along x_1^c in its local coordinate system $\boldsymbol{x^c}$ and the SW along x_1^s and parallel to the $x_1^s - x_2^s$ plane in its local system $\boldsymbol{x^s}$. Therefore, the CW-caused strain tensor, ε_{ij}^{cc}, is the uniaxial strain state in $\boldsymbol{x^c}$; i.e., except for ε_{11}^{cc}, other elements of ε_{ij}^{cc} are zero. The SW-caused strain tensor, ε_{ij}^{ss}, has only non-zero shear strains; i.e., all normal strains of ε_{ij}^{ss} are zero. Because the volumetric strain, ε_{ii}, is a constant and because SW cannot change volume, we always have $\varepsilon_{11}^{cc} = \varepsilon_{ii}$. While ε_{ij}^{cc} is determined, the propagation directions of CW and SW are unknown in fact. Define q_{ij}^{s} as the transformation matrix from $\boldsymbol{x}$ to $\boldsymbol{x^s}$ and q_{ij}^{cs} as the transformation matrix from $\boldsymbol{x^c}$ to $\boldsymbol{x^s}$, i.e. $q_{ij}^{s} = \cos(x_i^s, x_j)$ and $q_{ij}^{cs} = \cos(x_i^s, x_j^c)$, and apply q_{ij}^{s} to Eq. (8),

$$q_{mi}^{s} q_{nj}^{s} \varepsilon_{ij} = q_{mi}^{s} q_{nj}^{s} \varepsilon_{ij}^{c} + q_{mi}^{s} q_{nj}^{s} \varepsilon_{ij}^{s} \tag{9}$$

With the consideration of the analysis above, it can be established that $q_{mi}^{s} q_{nj}^{s} \varepsilon_{ij}^{c} = q_{mk}^{cs} q_{nl}^{cs} \varepsilon_{kl}^{cc}$ and $q_{mi}^{s} q_{nj}^{s} \varepsilon_{ij}^{s} = \varepsilon_{mn}^{ss}$, which makes Eq. (9) become

$$q_{mi}^{s} q_{nj}^{s} \varepsilon_{ij} = q_{mk}^{cs} q_{nl}^{cs} \varepsilon_{kl}^{cc} + \varepsilon_{mn}^{ss} \tag{10}$$

Because $\varepsilon_{mn}^{ss} = 0$ when $m = n$, the relationship can be derived through Eq. (10),

$$q_{mi}^{s} q_{mj}^{s} \varepsilon_{ij} = q_{mk}^{cs} q_{ml}^{cs} \varepsilon_{kl}^{cc} \tag{11}$$

which reveals a clue that the propagation direction of SW can be found if q_{ij}^{s} and q_{ij}^{cs} are determined.

With given ε_{ij} and ε_{kl}^{cc}, q_{ij}^{s} and q_{ij}^{cs} can be sorted out by rotating $\boldsymbol{x}$ and $\boldsymbol{x^c}$, independently, until q_{ij}^{s} and q_{ij}^{cs} are matched each other to satisfy Eq. (11). This is the key idea of the proposed method in the Chapter. The specific procedures are as follows.

(i) Measure the displacement field and the vibration velocity field at all moments. In this procedure, interpolation may be implemented to have all positions displaced from the measured displacement field.

(ii) Calculate the strain from $\varepsilon_{ij} = (u_{i,j} + u_{j,i})/2$. Accordingly, ε_{ij}^{cc} is determined with ε_{11}^{cc} equal to ε_{ii} and other components equal to zeros.

(iii) Rotate $\boldsymbol{x}$ and $\boldsymbol{x^c}$ to all possible orientations of $\boldsymbol{x^s}$ with an angle step, independently, and record all corresponding transformations of ε_{ij} and ε_{ij}^{cc}. It is not necessary to try all possibilities in practice. In order to reduce the computation time, possible orientations should be estimated appropriately upon the real excitations producing SW and CW.

(iv) Compare each transformation of ε_{ij} with each one of ε_{ij}^{cc} and determine the best pair of q_{ij}^{s} and q_{ij}^{cs} making $\sum_{m=1}^{3}(q_{mi}^{s} q_{mj}^{s} \varepsilon_{ij} - q_{mk}^{cs} q_{ml}^{cs} \varepsilon_{kl}^{cc})^2$ minimum.

(v) Deduce the CW-based vibration velocity from the determined q_{ij}^{s} and q_{ij}^{cs}. The vibration velocity in $\boldsymbol{x}$ can be transformed to $\boldsymbol{x^s}$ by

$$v_i^{s} = q_{ij}^{s} v_j \tag{12}$$

where v_j is the vibration velocity in $\boldsymbol{x}$, v_i^s is the vibration velocity in $\boldsymbol{x^s}$. The vibration direction of SW is perpendicular to x_1^s, from which v_1^s in Eq. (12) is the only component of the CW-caused motion. Consequently, the CW-caused vibration velocity, $\dot{u}_1$, and the corresponding volumetric strain, $u_{1,1}$, in $\boldsymbol{x^c}$ are untangled out of the combined strain field by

$$\dot{u}_1 = v_1^s / q_{11}^{cs} \tag{13}$$

$$u_{1,1} = q_{1i}^s q_{1j}^s \varepsilon_{ij} / (q_{11}^{cs} q_{11}^{cs}) \tag{14}$$

It is noted that $u_{1,1}$ is ε_{11}^{cc}. There could be numerical error between them. For having all data analyzed consistently with measurement, Eq. (14) is used. Based on the deformation gradient of shear motion that is asymmetrical, SW-caused strain and vibration velocity can be determined with the known CW-caused ones from Eq. (13) and Eq. (14).

(vi) Map elastography by solving V with substituting Eq. (13) and Eq. (14) into Eq. (7). The measurement is a set of discrete data within a certain period of time. For reducing the noise effect and making use of all measured data, Eq. (7) can mathematically and generally be reorganized as,

$$V = \sqrt{\frac{\sum_{t=1}^{t=t_n} \dot{u}_i^2}{\sum_{t=1}^{t=t_n} u_{i,j}^2}} \tag{15}$$

where t_n is the number of the collected data. Young's modulus or shear modulus can further be obtained through Eq. (2) or (6). In fact, the numerator and the denominator of Eq. (15) can be understood as the autocorrelations of $\dot{u}_i$ and $u_{i,j}$ at zero lag, respectively.

4.3 Validation

To demonstrate the performance of current study, numerical models are built for forward analysis, followed by the inverse reconstruction. The first model (9.0 cm × 5.0 cm with a 1.5 cm inclusion embedded) is a two-dimensional case in which the 300 Hz shear excitation is set on the top surface of the sample and fixed on the bottom [144]. The shear modulus of matrix is 40 kPa and the inclusion is 15 kPa. Poisson's ratio is assumed to be 0.49. The densities of the matrix and inclusion are assumed to be 612 kg/m^3 and 1000 kg/m^3, respectively, making the shear-wave impedances of the matrix and inclusion identical or matched. Using the commercial finite element analysis package, COMSOL, the wave motion is simulated with 0.1 cm quadrilateral elements of plane strain. The excitation lasts 0.03 s with the time step of 5×10^{-5} s. It is noted that, while plane-strain case is assumed in the COMSOL forward analysis, the algorithm for elastography reconstruction does not require whether the problem is a plane-strain or a plane-stress case, since such information is intrinsically embedded in the displacement data. With the conventional SWE method directly measuring the wavelength through the displacement distribution that is used to estimate the wave speed [144], the position of inclusion can be detected, whereas the geometrical shape cannot, as shown in Fig. 23 (a). When the current study is applied to the same displacement field, not only can the inclusion location be located, but the shape be identified as shown in Fig. 25 (b). In the procedure (iii), the rotation step of each axis is $\pi/120$ and the searching range is $[0, \pi/2]$, which takes 2.5 hours of computation on a PC with Intel(R) Core (TM) i7-3770 CPU @ 3.40 GHz. After the density of matrix is assigned 1000 kg/m^3 that makes impedances mismatched and induces reflections and mode conversion at the interface between matrix and inclusion, the displacement difference is

subtle compared with Fig. 25 as shown in Fig. 26. Due to the mismatched impedance that produces tangled deformation of SW and CW near the interface, the inclusion can hardly be targeted by the conventional SWE method of measuring the wavelengths as shown in Fig. 26 (a). In other words, the tangled field will mislead the measurement of wavelengths. When the current study is implemented, the inclusion still can clearly be identified even with reflection occurrence as shown in Fig. 26 (b).

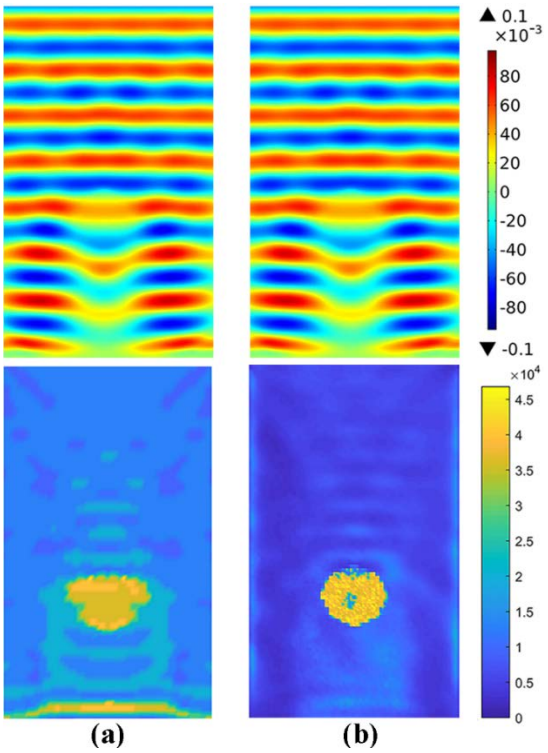

Fig. 25. Matched impedance case: Displacement distribution in cm (top) and corresponding elastography of shear moduli in Pa (bottom): (a) by conventional SWE and (b) by the current method

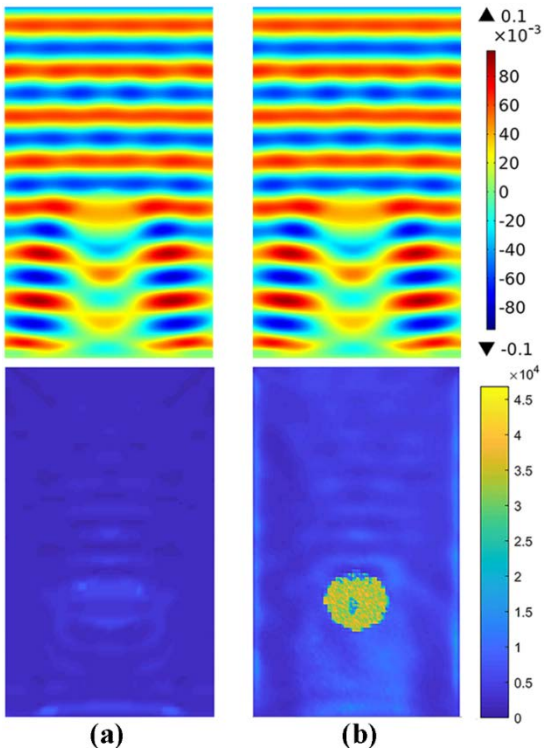

Fig. 26. Mismatched impedance case: Displacement distribution in cm (top) and corresponding elastography of shear moduli in Pa (bottom): (a) by conventional SWE and (b) by the current method

The second example, 15 cm × 8 cm, is a four-inclusion case as shown in Fig. 27 (a) on which the arrows denotes the positions acted with the 1 Hz sine displacement excitation. The displacement excitation is expected to generate a CW-SW tangled field. The

diameters of inclusions are all 2 cm. Young's moduli are 25 kPa for the matrix and 8 kPa, 14 kPa, 45 kPa and 80 kPa for inclusions as marked on Fig. 27 (a) [73]. The density is assumed 1000 kg/m^3 and Poisson's ratio is 0.49 for all materials, which yields 20.7 m/s CW velocity to the matrix, 11.7 m/s, 15.5 m/s, 27.8 m/s and 37.0 m/s to inclusions. Obviously, the wavelengths are tens of meters under 1 Hz. The model is meshed with 10040 triangular elements of plain strain. During the simulation, the left boundary is fixed, and the exciting duration is 0.5 s with the time step of 5×10^{-3} s. Thereafter, the velocity and strains are exported to trigger the procedures (i) ~ (vi). After q_{ij}^{s} and q_{ij}^{cs} are found, the elastography is mapped with the distribution of Young's moduli through Eq. (15) and Eq. (6) as shown in Fig. 27 (b) with the computation time of 12 minutes. It is illustrated that the inclusions are clearly differentiated with sharp interface identification. The reconstructed Young's moduli of four inclusions are 8.0±2.0, 14.0±3.5, 45.0±7.6 and 80.0±15.9 in kPa. Although the CW wavelength is far greater than the inclusion size and the model dimension under 1 Hz, the current method works well. It is impossible for the traditional SWE to map moduli by directly measuring such long wavelengths under 1 Hz. This further promotes the current study valid for low frequencies which make waves penetrate deeper with low attenuation. In addition, the low frequency wave will not deliver a resolution loss because the present study centers on deformation, not on wavelength. To show that the method does not depend on the frequency, one more image under 100 Hz are simulated and reversely mapped as shown in Fig. 27 (c), which agree with the image of 1 Hz. For further showing the capacity and uniqueness of the proposed method, if the stimulus of Fig. 27(a) is set to be perpendicular to the right surface under 100 Hz making the traditional SWE useless, the corresponding elastography is mapped in Fig. 27(d) that is consistent with Fig. 27(c).

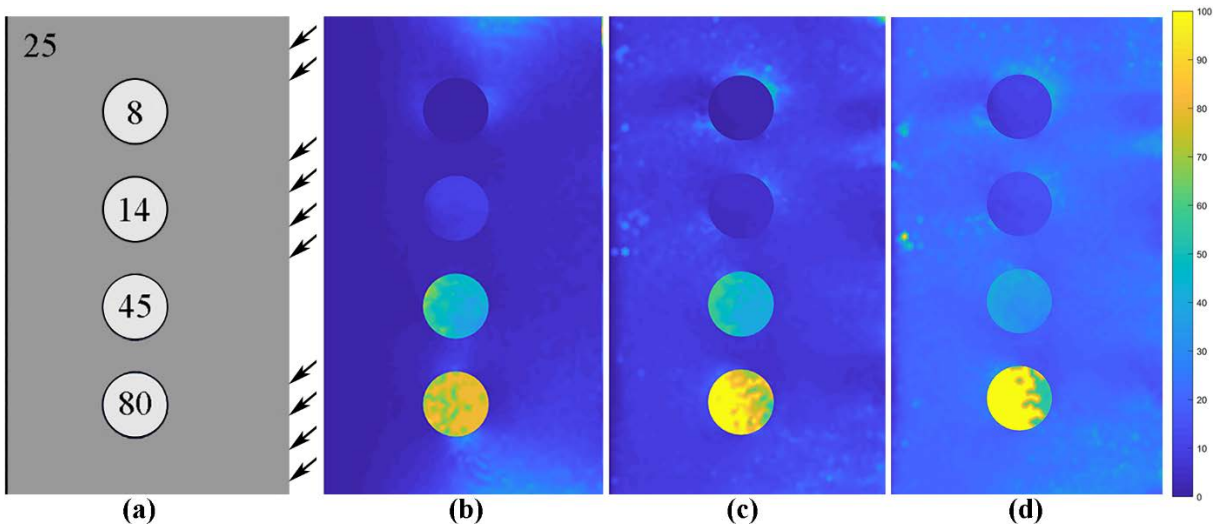

Fig. 27. (a) The 2D model with 4 circular inclusions of the 2 cm diameter, (b) - (c) Young's modulus elastography images reconstructed by the current method under 1 Hz and 100 Hz, respectively, and (d) elastography under 100 Hz with the excitation perpendicular to the right surface in the model.

To demonstrate the sensitivity of current algorithm to noise, all fields of Fig. 27(c) are added artificially with the white noise of signal-to-noise-ratio (SNR) of 55 dB and 60 dB, respectively. Fig. 28(a) shows the typical displacement of a point with noises. Compared with Fig. 27(c), the elastography is acceptable with the 60 dB noise imaged in Fig. 28(b) despite existing errors at some points, but not with 55 dB noise even if the interfaces are sharp as shown Fig. 28(c). Therefore, it is recommended that the data need to be filtered or smoothed if SNR is down to 60.

It is noticeable that they are not strictly two independent plane waves (CW and SW) passing each point throughout each model of the two demonstrations in terms of wave scattering and multiple excitations. For example, there are three sources in the second demonstration. But sticking to the fact that any volumetric strain can just be produced by CW, the deformation of a point can always be decomposed into a CW-caused component and a SW-caused component if the wave numbers are same from all sources. If the wave

numbers of sources are different, a central frequency may need to be estimated first for making Eq. (7) realizable and then, the proposed study can be employed.

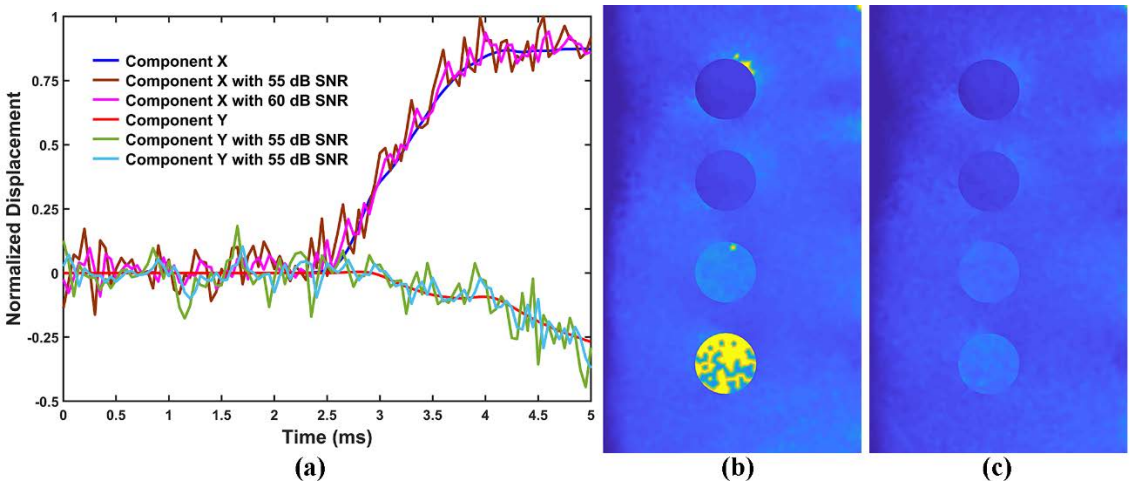

Fig. 28. (a) Displacement with noise and (b) - (c) elastography images with SNR of 60 dB and 55 dB, respectively.

4.4 Conclusion

An elastography method is developed that aims at untangling compression-shear field by rotating strain tensor. With simply measuring a displacement field over time, the region of interest can be mapped with the stiffness distribution. Demonstrations show that the method can identify the heterogeneous inclusions clearly and map the modulus distribution accurately. The Chapter provides an effective and executable path for clinical imaging in healthcare practice.

Chapter 5 Microstructural Origins of Wave Modulus of Composites

5.1 Introduction

Ultrasound-based methods have been widely used to evaluate the mechanical properties of composite materials. For example, the elastic modulus can be assessed according to the measured velocity of wave propagation [78]–[82]. The estimation of elastic modulus or modulus of elasticity comes from the well-known relationship of Eq. (2) rewritten as,

$$V_s = \sqrt{\frac{E_w}{2(1+\nu)\rho}} \tag{16}$$

where E_w is called wave modulus (WM) in the Chapter. In practice, the time of flight (TOF) of wave is measured through the input and transmitted signals [82], [159]. For homogeneous materials, E_w is equal to the elastic modulus, i.e., the Young's modulus. In contrast with the static uniaxial compression testing, the distinct advantage of the pulse velocity test is nondestructive and easy to perform in-situ. There are a few terminologies regarding wave-velocity-based modulus estimation, such as pulse modulus, dynamic modulus, and wave modulus. In this study, the term of wave modulus (WM) of elasticity is used.

When either the direct transmission or surface transmission is currently performed practically, WM relies on the wave velocity estimation while avoiding the material heterogeneity on the propagation path [159]–[161]. Due to the composite nature of concrete materials even with exiting voids, the heterogeneity takes effect in both microscale and macroscale. So far, investigations have been conducted, using the analytical micromechanics principles and experiments to reveal the effect of heterogeneity not only

on the static modulus of elasticity [162]–[164], but on the wave propagation [165]–[168]. It needs to be pointed out that current discussion is under the requirement of separation-of-scales, namely, $d \ll \mathcal{R} \ll \lambda$ (where $\mathcal{R}$ is the characteristic length of the representative volume element (RVE), d is the characteristic length of heterogeneities in RVE and λ is the wavelength) [168], [169]. While those analytical explorations are limited to inclusions of regular shape, some fundamental conclusions have been reached. First, the influence of inclusions on the propagation path is coupled with wavelength or frequency. Second, the product of the wave number and the inclusion radius, ka (where k is the wave number equal to $2\pi/\lambda$ and a is the inclusion radius), is a useful parameter to better understand their coupling mechanisms. If the wavelength is much greater than the characteristic length of inclusions, it has limited sensitivity to the inclusions scale. When $ka \to 0$, WM tends to be the corresponding static modulus of elasticity. If the wave frequency makes $ka \to 1$, i.e., the inclusion size is in the same order as the wavelength, the propagation starts showing wavelength dependence. With increase of ka, when $\lambda < d$, the wave can have multiple interaction with a single inclusion during propagation, which is beyond the scope of current discussion. Third, for the cases of stiffer inclusions, WM is less than the static modulus of elasticity in relatively low ultrasound frequencies because of wave scattering, in which the wavelength is larger than the aggregate scale. In WM testing, with considering the frequency dependent attenuation, the required frequency is set on the order of 100 kHz [82], [159]–[161], [167]. Taking concrete as an example, in the range of such frequency, the wavelength of concrete is $\sim 10^1$ mm that is larger than fine aggregates. Therefore, mortar that is the mixture of fine aggregate and cement can be treated as homogeneity [170]. For coarse aggregates and voids, the frequency causes $ka \sim 1$ that is approved to affect wave

motion. It has been reported that WM of concrete is up to 30% higher than its corresponding static modulus of elasticity based on both longitudinal and shear wave excitations [78], [82], [83], which seems to contradict with the aforementioned third conclusion. Because aggregates and voids of concrete are of irregular shapes, there are no analytical solutions available to predict their effects on the overall elastic properties of concrete. The analytical analysis with the assumption of regular shapes could only present some basic ideas, but not the full picture. Numerical solutions through finite element method (FEM) is anticipated to provide more insight because FEM is free of the inclusion shape restriction and sheds light on studying complex heterogeneous multi-phase concrete [170]–[172]. Furthermore, realistic microstructures of concrete can be resolved by utilizing the state-of-the-art imaging technologies such as X-ray microscopic computerized tomography (micro-CT) [173]–[175]. The integration of FEM and the micro-CT imaging technology helps bridge the microstructural features of concrete and its macroscopic mechanical performance. The current study is among the first efforts to investigate the microstructural origins of WM of concrete by combining the computational micromechanics and micro-CT technology.

In this Chapter, with the treatment of concrete as a three-phase composite material (aggregates, mortar and voids), effect of aggregates on WM is first studied using FEM to simulate shear-wave motion. In this part, the aggregate with $ka \sim 1$ is analyzed and approved that its presence is not the reason causing higher WM. In addition, different ka values, i.e. different λ/d, are disused. Second, the effect of voids is investigated and approved that crack-like voids are the reason causing higher WM. In this part, aspect ratio is specially analyzed and concluded that smaller aspect ratio makes faster drop of static

modulus than of WM. Finally, the wave velocity analysis is performed on the real concrete structures resolved with micro-CT.

5.2 Effect of Particle Inclusions

In this section, the role of particles in wave motion is analyzed using the microstructure-based finite element method (FEM). To ensure the simulation accuracy, at least ten nodes are introduced with a wavelength in developing finite element mesh. Further, the incremental time step is less than the propagation time passing through a single element [106], [171]. A commercial FEM package, *Marc Mentat* 2017 (64 bit) (MSC Software Corporation), is used to conduct all simulations. The input signal is the acceleration excitation of a half-sine pulse of 100 kHz. In an idealized homogeneous material with no consideration of microstructures, WM depends on the time of flight (TOF) between two points that one serves as the source (e.g., transmitter) and the other as the detection (e.g., receiver). The velocity evaluated from the TOF between any two points is simply a constant. However, for heterogeneous concrete, the wave velocity can locally be path-dependent because of the aggregate variation. To demonstrate the local path-dependence of aggregates, three plane-strain cases are modeled. The first two are a triangular aggregate of 6.7 mm size as shown in Fig. 29 (a) and a circular aggregate (area unchanged) embedded in a matrix of 102 mm × 120 mm, respectively, while the third one is a homogeneous matrix-only case as a reference. The three models are meshed with 11332 triangular elements with the maximum edge of 1.5 mm that is 1/10 (or finer) of wavelength. The triangle is represented by 28 elements and the circle by 36 elements. The basic property input includes the elastic modulus of 14 GPa, density of 2200 kg/m^3, and

Poisson's ratio of 0.17 for the matrix, and the elastic modulus of 45 GPa, density of 2690 kg/m^3, and Poisson's ratio of 0.17 for aggregates. The excitation of the half-sine pulse is set near the left end as denoted by arrows in Fig. 29. The time increment per step is 0.25 μs (which is about 27% of time traveling within a matrix element and 42% within an aggregate element). Upon the completion of simulation, the typical acceleration contours are illustrated at the moment of 25 μs in Fig. 29 from which the wave front and the reflection of boundaries can be observed. The model size can allow the front to reach the right boundary first without interfering with the boundary reflections. To reveal the difference among the three cases, the accelerations normalized by the maximum absolute value are plotted in Fig. 29 (b) along the wave propagation centerline. It shows that the difference emerges and presents the shape effect apparently. In relation to the WM evaluation, the first peak head is the only interest used to estimate the TOF between the two peaks of the input and the transmitted signal. Specifically, TOF is estimated by subtracting the quarter period of the input signal from the first peak moment of the transmitted signal, followed by the determination of the wave velocity by dividing the distance between the excitation source and the receiver by TOF. Thus, WM is obtained through Eq. (16). Estimated from Fig. 29 (b), the normalized WMs are 1.00, 1.08 and 1.13 for the no-aggregate (matrix-only) case, the circular one and the triangular one, respectively. Although the areas of the triangle and the circle are same, i.e. the same volume fraction, the triangular aggregate delivers a faster motion because of more occupation on the wave path and has larger effective ka. WM of the triangular case is 4.6% higher than WM of the circular one, showing that the triangular orientation affects the WM estimation. If the wave propagates right along one triangular side, it reaches 5.0% higher than WM of

the circular particle. The difference may exist in their corresponding static moduli. Even if their static moduli of elasticity are the same, the 5.0% cannot eliminate the large 30% gap between WM and the static counterpart.

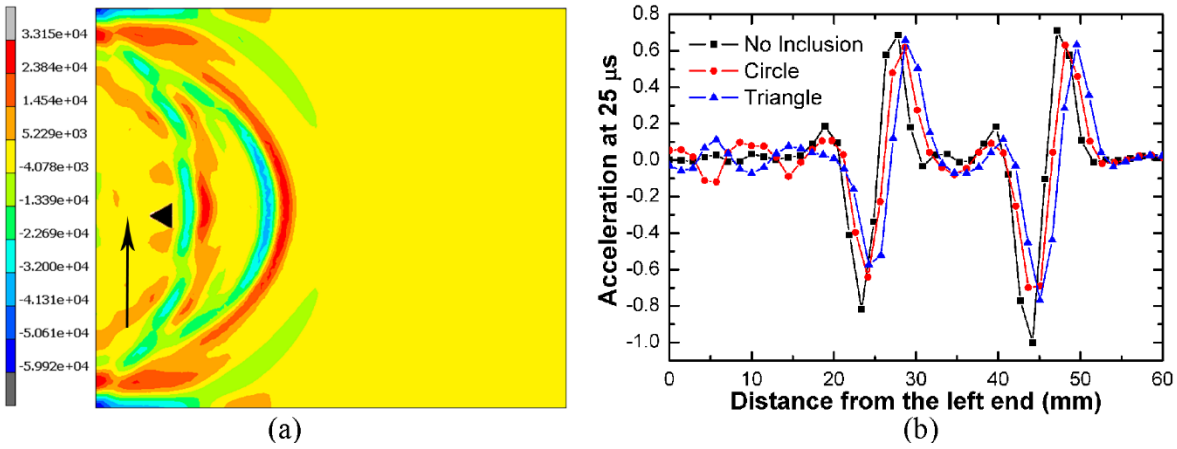

Fig. 29. Acceleration (mm/s²) contour bands at 25 μs with (a) a single triangular aggregate and (b) the propagation comprison of three cases along the propagation centerline at 25 μs

Real concrete materials contain many aggregates. In fact, the existence of aggregates causes lower WM than the static counterpart. If a 30% volume fraction of 5 mm diameter aggregates is embedded in the matrix as shown in Fig. 30 (a), the simulation results show that the WM is lower than the static as shown in Fig. 30 (b). Boundary conditions of Fig. 30 (a) are set free, except that the two end points of the left boundary are fixed. The half-sine excitation is set at the center on the left boundary. In the simulation, the time increment of 0.25 μs is determined through comparison with other increments as shown in Fig. 31 (a). It is shown that the increment starts to converge below 0.4 μs although the time passing through an element is ~ 1 μs. For all simulations in the current study, the time step is chosen as 1/4 of the time length passing the element. The loading position of excitation is set at the center of the left boundary. To demonstrate the chosen model satisfying RVE

requirement, the loading is also applied with different positions within $\pm 5a$ (a is the radius of the inclusion) around the center of the boundary. The results illustrated in Fig. 31 (b) indicate that the times having the peak front are consistent, only causing WM errors within 1%, although the amplitudes are variable due to scattering. Furthermore, the position change leads to the wave path different which can be understood on different random generalizations of the inclusion distribution. Up to 50% volume fraction of aggregates, normalized by the elastic modulus of the matrix, the tendencies of WM and the static modulus are plotted in Fig. 30 (b). It is shown that WM becomes smaller than the static modulus of elasticity with the increase of the volume fraction of aggregates. For the sake of demonstrating the effect of changing frequency, Fig. 33 shows the normalized WM by the static modulus with different λ/d and demonstrates that the WM variation is subtle in the frequency range of WM; yet the WM is always lower than the static modulus. To further demonstrate the aggregate irregularity in concrete, an X-ray microscopy slice of the natural aggregate concrete is segmented and meshed as shown in Fig. 33. The simulation of wave motion and comparison are conducted on two directions, which reports the static modulus of 19.68 GPa and WM of 15.27 GPa on the horizontal direction, and the static modulus of 19.29 GPa and WM of 17.59 GPa on the vertical direction. The two static moduli are consistent. WM values reflect the path dependence, but lower than related static moduli. Based on the analysis, the aggregate existence is not the reason causing higher WM.

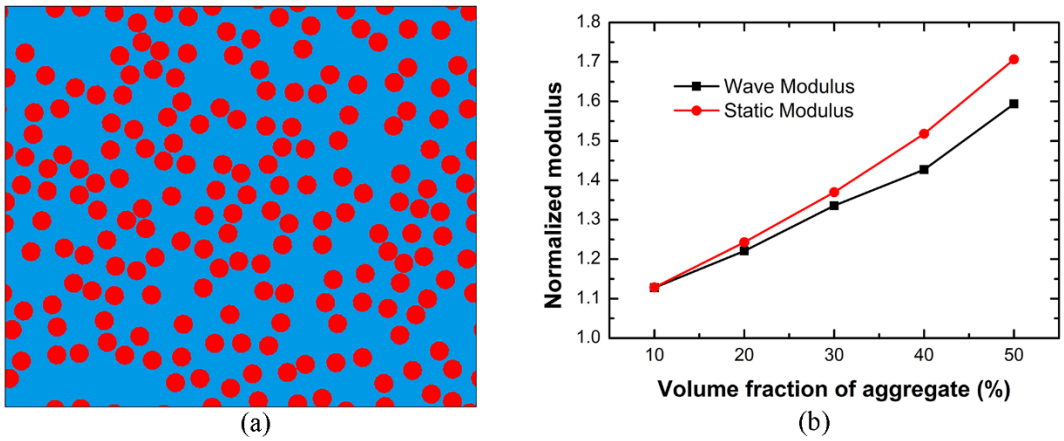

Fig. 30. (a) Concrete microstructure with 30% volume fraction of aggregates and (b) the comparison between the WM and static modulus of elasticity of concrete as a function of volume fraction of aggregates

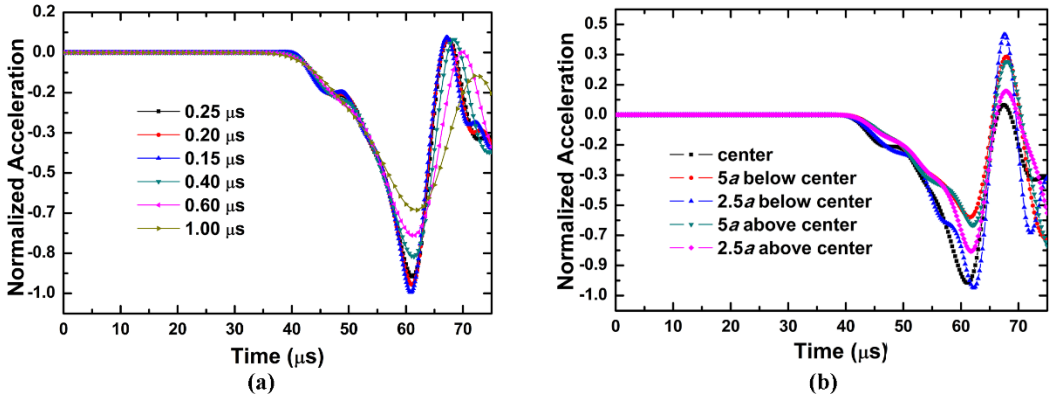

Fig. 31. (a) The comparison of different time increments and (b) comparison of loading positions

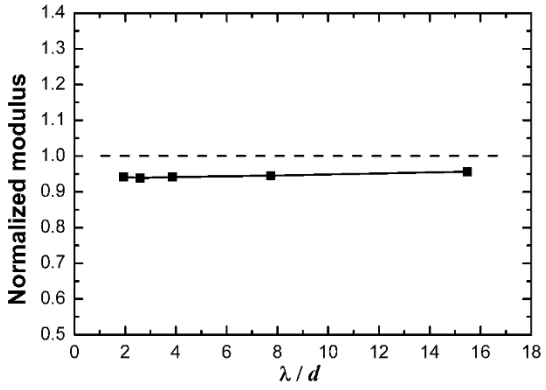

Fig. 32. WM with different λ/d values

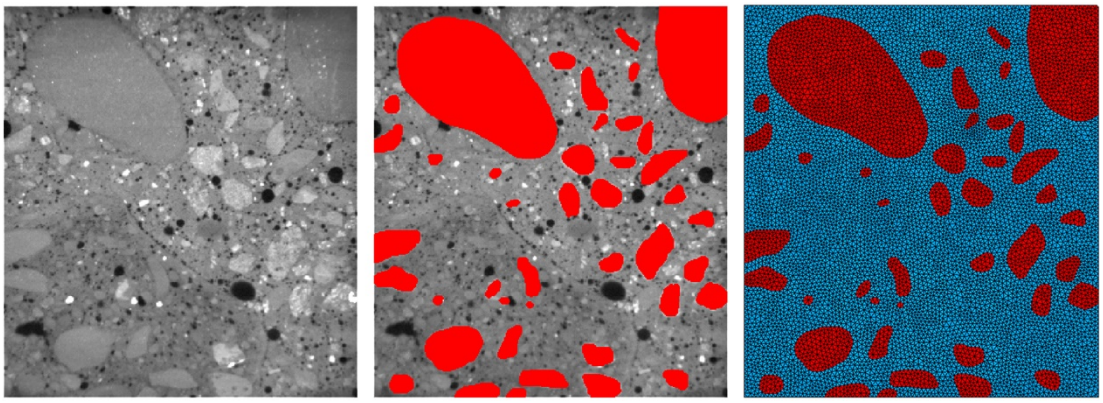

Fig. 33. An X-ray CT resolved concrete slice (17.2 mm × 18.9 mm), segmented aggregate (30% volume fraction) and finite element mesh with no consideration of voids

Lower WM due to the presence of aggregates can be interpreted by the wave refraction. Known from wave's characteristics [95], if the wave incidence is not on the direction of the interface normal of two media, the refraction occurs and its angle is not equal to the incidence angle. From this point of view, refraction tends to change the propagation direction and makes the travel path not in a straight line between two points, but in polylines. Because the length of polylines is longer than that of a straight line, the propagating velocity under the assumption of the straight line thus leads to an underestimation of wave modulus of elasticity. This also concludes that the higher WM does not result from its sensitivity to aggregates.

5.3 Effect of Voids

Different from particles, micro-voids reduce elastic modulus of material. If voids are spherical and evenly distributed, the similar analysis process can be conducted as done for aggregates, and the similar conclusions can be drawn that spherical voids are not the reason causing higher WM. For example, if the volume fraction of 2-mm-diameter void is

5% in a 2D model (with the RVE of 102 mm by 120 mm), the normalized static modulus of elasticity is 1, whereas the WM is 0.88 under both 10kHz and 50kHz, corresponding to λ/d~8 and λ/d~16, respectively. Within RVEs, the propagation path is the presentative of cross-section based on which the static modulus is determined. The tendency in 2D simulations may be applied to 3D cases.

Based on the above analysis, both aggregates and spherical voids are not the reasons causing higher WM. They make WM and static modulus of elasticity varying synchronically. Furthermore, WM is smaller than the corresponding static modulus of elasticity. In real concrete, all voids are not possible in spherical shape. There is a need to investigate the effect of non-spherical voids such as crack-like voids. For a cracked solid [176], [177], the elastic modulus is the function of the crack density that can be defined as,

$$c_d = \frac{2N}{\pi} < \frac{A^2}{P} > \tag{17}$$

where c_d is the crack density, N is the number of cracks per unit volume, A is the area of crack, P is the perimeter of crack, and $< >$ denotes the volume average of the quantity. For 2D cracks, the crack density is computed accordingly as,

$$c_d = \frac{8}{\pi^3} M < l >^2 \tag{18}$$

where M is the number of cracks per unit area, and $< l >$ is the average trajectory of the cracks [176], [178]. It is noticed that the effect of cracks on the static modulus of elasticity is associated with the order of the third power of the crack size for 3D and the second power for 2D. However, WM is just associated with the first power of the crack length, i.e., ka, which implies higher WM. In addition, both c_d and ka are directly linked to the length a, instead of the porosity. High crack density can reduce the elastic modulus severely [176], [178], [179]. For concrete, the crack density depends on the compression stress level

because higher stress will induce more microcracks and initiate existing cracks to propagate. At the initial status of zero stress, the crack density of cementitious materials is above 0.2 [178]. Based on Eq. (18), the crack density of 0.2 is modeled with the 8 mm long cracks of random distribution, as shown in Fig. 34. Through FEM simulation, the normalized WM by the corresponding static modulus of elasticity is 1.49, which is 49% higher than the static modulus. In this simulation, the boundary conditions are set as the same as those in Fig. 29. It seems clearly that crack results in the larger decrease of the static modulus of elasticity. In other words, the existence of crack leads to higher WM. It needs to be pointed out that the volume fraction of crack-like voids is only 1.5% in the model as shown in Fig. 34. If the 1.5% volume fraction counts on spherical voids, the conclusion is totally different, being lower WM.

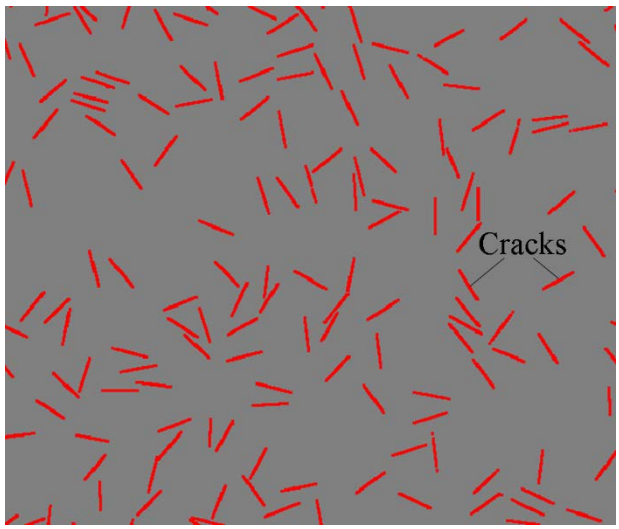

Fig. 34. FEM model of concrete with randomly distributed cracks

However, spherical voids and cracks are the two extreme ends. One end presents higher static modulus and the other does higher WM. Even if the crack density is constant, the wave velocity will decrease with respect to the extent of crack opening [180]. This phenomenon is anticipated because wider crack gives higher volume fraction. Obviously,

the aspect ratio of a void, being the scenario between crack and spherical void, plays the role manipulating the difference of WM and its static counterpart, which can be illustrated in Fig. 35 with the void volume fraction (porosity) of 5%. The void shape is elliptical. It can be seen that the static modulus drops dramatically with the smaller aspect ratios. Although WM has the same tendency, it has the same value as the static modulus at about 0.2 aspect ratio and starts being larger below 0.2. It is noted that WM does not change smoothly, which may be because of the strong nonlinear interactions among wave motion, aspect ratio and the number of voids. The discussion about this is beyond the scope of current study. However, one thing is confirmed that WM is always lower than its static counterpart above a specific aspect ratio, and higher than the static counterpart below the specific ratio. The voids with aspect ratios smaller than a specific value are identified as crack-like voids because they cause higher WM. The voids above the specific aspect ratio are called as round voids because they cause lower WM like ideally spherical voids.

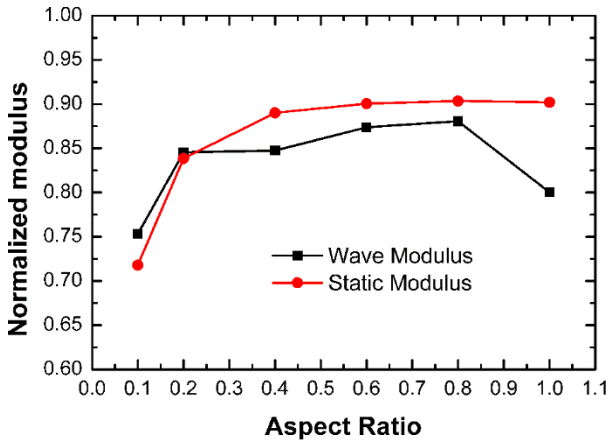

Fig. 35. Comparison of WM and its static counterpart with different aspect ratios

In reality, however, the void configuration is commonly irregular and cannot be simply delineated by an ellipse and an ellipsoid. For example, as shown in Fig. 36, it is difficult to use the aspect ratio to quantify the real void that is detected by X-ray micro-CT.

Another parameter, sphericity, is thus suggested to deal with the irregular void [181]. Sphericity, s, is defined as,

$$s = 6\sqrt{\pi}\frac{V_s}{\sqrt{A_s^3}} \tag{19}$$

where V_s is the void volume and A_s the surface area. For the ideal sphere, $s = 1$, and for the ideal penny shape crack, $s = 0$. Accordingly, for 2D problems, the roundness can be defined as,

$$r = 4\pi\frac{A}{C^2} \tag{20}$$

where r is the roundness, A is the area and C is the circumference. For the ideal circle, $r = 1$, and for the ideal crack, $r = 0$. If Eq. (20) is applied to the case with the specific aspect ratio 0.2 as shown in Fig. 7, $r = 0.45$, meaning that roundness below 0.45 tends to generate higher WM.

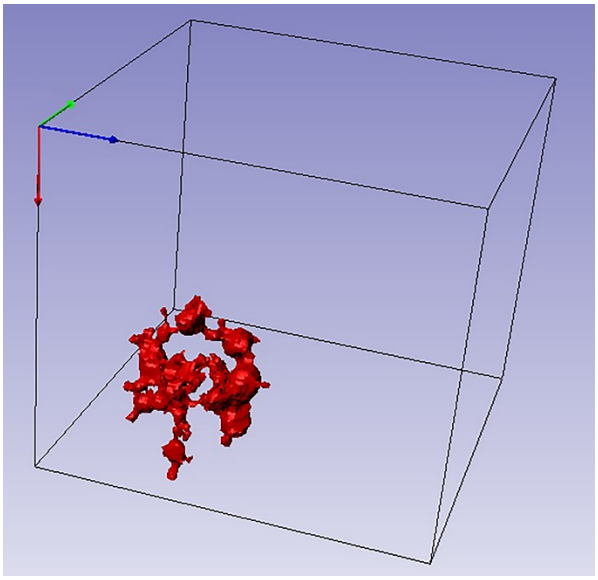

Fig. 36. A real void detected by X-Ray micro-CT that can be characterized by sphericity rather than aspect ratio

5.4 Simulation on real concrete structures

In order to strengthen the conclusion that higher WM is attributed to crack-like voids, two concrete samples are imaged by X-ray micro-CT, followed by FEM simulations. The CT scanner is *Xradia 410 Versa* (Carl Zeiss X-ray Microscopy, Inc.) that has the best spatial resolution of 0.9 μm. In the present study, the resolution is 25 μm. The two samples are the recycled aggregate concrete (RAC) and the natural aggregate concrete (NAC) [83]. For each concrete, the cubic specimen with approximate edge-length of 15 mm and prismatic specimen with dimensions of 50 mm by 50 mm by 100 mm are cut from the same laboratory-cast beam with dimensions of 75 mm by 100 mm by 400 mm. Cubic specimens are used in micro-CT scan and prismatic specimens in uniaxial compression testing. The X-ray CT images are shown in Fig. 37, showing internal structures of concrete. ScanIP®, a professional image processing product of *Simpleware LTD*, is employed to segment, measure and mesh all components of 3D concrete images.

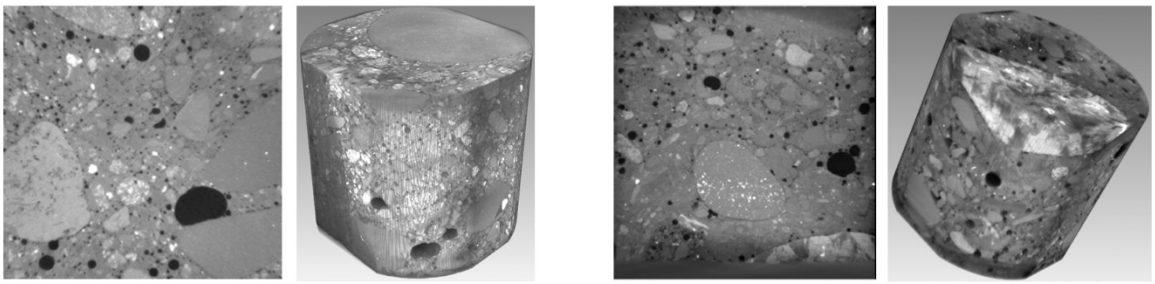

Fig. 37. Micro-CT images of RAC and NAC: (a) a typical slice of 15.8 mm × 13.9 mm and 3D image of NAC, and (b) a typical slice of 13.1 mm × 14.8 mm and 3D image of RAC

According to these CT images, the difference between RAC and NAC cannot be visually identified. It has been characterized that RAC has less elastic modulus, lower density, and greater water absorption than NAC [83]. Scales of voids below 0.1 mm are not

counted, and the measured volume fraction of voids is 5.6% for NAC and 5.2% for RAC as shown in Fig. 38. During segmentation, only is the aggregate above 1.5 mm picked out, which shows the volume fraction of aggregate of 28.2% in NAC and 33.9% in RAC. Smaller aggregate is merged into mortar treated as a part of the matrix because they are not expected to affect WM under current wavelength. The size of aggregates ranges from 1.5 mm to 8 mm, which is less than the wavelength amounting to ~20 mm. Although the requirement of separation-of-scales is not strictly satisfied [168], [169], the expected error is less than 1.8% as shown in Fig. 32. This level of accuracy is sufficient for the present study. Because of microstructural features inside concrete, the final mesh is reasonably dense as shown in Fig. 38.

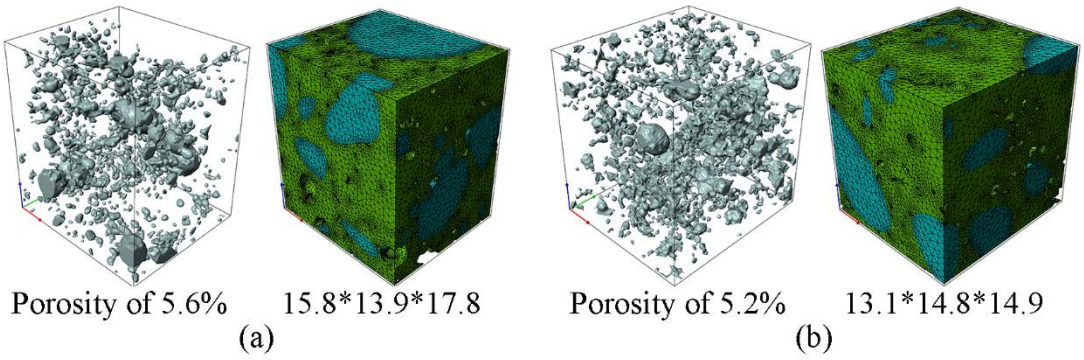

Fig. 38. Microstructural voids and FEM mesh of (a) NAC and (b) RAC concrete materials

Before FEM simulation, the two kinds of concrete properties are measured by uniaxial compression testing. The corresponding elastic static moduli are tested on the prismatic specimens using a MTS machine [182]. Two LVDTs with 2-inch gauge length are oppositely mounted on specimen surface to measure the compressive strain. To enable compression under quasi-static state, a very low loading rate (i.e., 0.1 mm/min.) is chosen. The measured elastic static moduli are 20.36 GPa and 16.85 GPa for NAC and RAC, respectively, extrapolated from compressive stress-strain curves as shown in Fig. 39.

Although cement paste is viscoelastic in nature, identification of the elastic Young's modulus from quasi-static tests on cement pastes (by accounting for both elastic and creep deformation during loading) delivers virtually the same stiffness values as ultrasonic testing [183]. With added aggregates, the WM will be below the static modulus as discussed in aforementioned analysis, indicating that viscoelastic nature is not the reason causing higher WM. In addition, the creep evolution of concrete is significantly slower than its stiffness [184]. However, there is no apparent relaxation in Fig. 39, which shows that the samples are nearly mature in creep evolution. Then, the material properties' input of FEM can be estimated based on the measured elastic static moduli. Initial rough estimations follow the rule of mixtures [185] and, then, use the trial-and-error method to match with the measured elastic static moduli. Input of material parameters are listed in Table 4. The final resultant homogenization moduli are listed in Table 5 in which errors compared with experiments are shown in parentheses. During the simulation, the symmetric boundary conditions are assigned to each model.

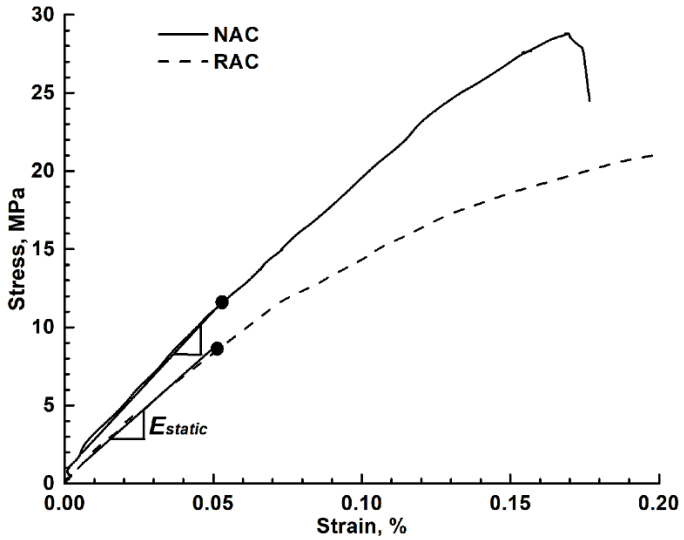

Fig. 39. Stress versus strain curves of compression test of NAC and RAC samples

Table 4. Material parameters of NAC and RAC

Parameter	NAC		RAC	
	Aggregate	Mortar	Aggregate	Mortar
Elastic modulus (GPa)	33.0	19.3	25.6	16.4
Density (kg/m^3)	2337	2337	2262	2262
Poisson's ratio	0.15	0.15	0.15	0.15

Table 5. Simulation results of RAC and NAC

Concrete	Static modulus of elasticity (GPa)			Wave modulus of elasticity (GPa)		
	Experiment	FEM		Experiment	FEM	
		With voids	Without voids		With voids	Without voids
NAC	20.36	20.41 (-0.25%)	23.74	23.11	23.08 (0.13%)	23.85
RAC	16.85	16.98 (-0.77%)	19.10	18.81	18.22 (3.1%)	19.60

For RAC and NAC, the wave speed is around 2,000 m/s which results in a wavelength of around 20 mm with 100 kHz frequency. For FEM models shown in Fig. 37, the wavelength is larger than the boundary scale, which influences the wave velocity [161]. Therefore, three dimensions of both RAC and NAC models are doubled by symmetric duplication. With applying symmetric boundary conditions, four original images are piled up together. Totally, the RAC FEM model contains 8,069,700 tetrahedral elements and 1,547,822 nodes, while the NAC model contains 7,130,676 elements and 1,348,910 nodes. The time step is 0.25 μs which satisfies the accuracy requirement of numerical simulation. Both computations take more than 48 hours per job for WM estimation, running in a 4-core i7 CPU and 16 GB memory PC. Wave pulse is applied at the center of an outer surface and the transmitted data acquired on the opposite surface. The propagation velocity is

estimated by comparing the input signals with its transmitted signals. Thereafter, WM is calculated based on Eq. (16).

Except the simulation on real concrete, the simulation with all voids removed and merged into the matrix is performed as the comparison origin. All simulation results and the static measurement are tabled in Table 5 and graphed in Fig. 40. The experimental WMs are obtained from Qiao 2010 that reported how to measure WMs in detail. It can be seen that the simulated WMs agree well with the experimental ones and are larger than corresponding elastic static moduli by 13.1% for NAC and by 7.3% for RAC. Taking the results without voids as the reference, the simulated WM is reduced by 3.2%, and the static modulus of elasticity by 14.0% for NAC, and by 7.0% and 11.1% for RAC. Both NAC and RAC results verify that the static modulus of elasticity decreases larger. To verify whether or not these higher WMs of NAC and RAC are attributed to crack-like voids, the probability density functions of sphericity of NAC and RAC are computed in terms of the micro-CT images and Eq. (19) as shown in Fig. 41. It can be seen that all voids are not ideal spheres and have sphericity mostly in range of 0.2 to 0.6. It is further validated that higher WM must be caused by non-spherical pores.

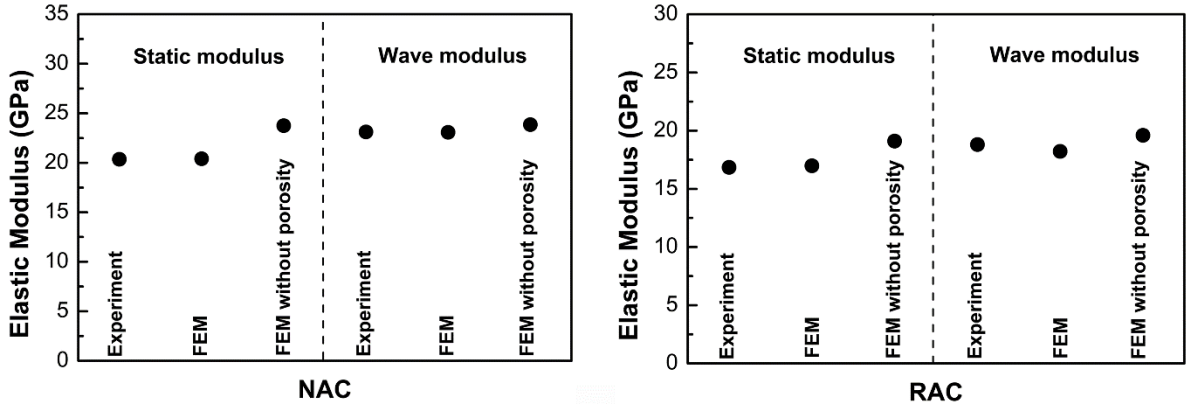

Fig. 40. Experimental and FEM results of NAC and RAC

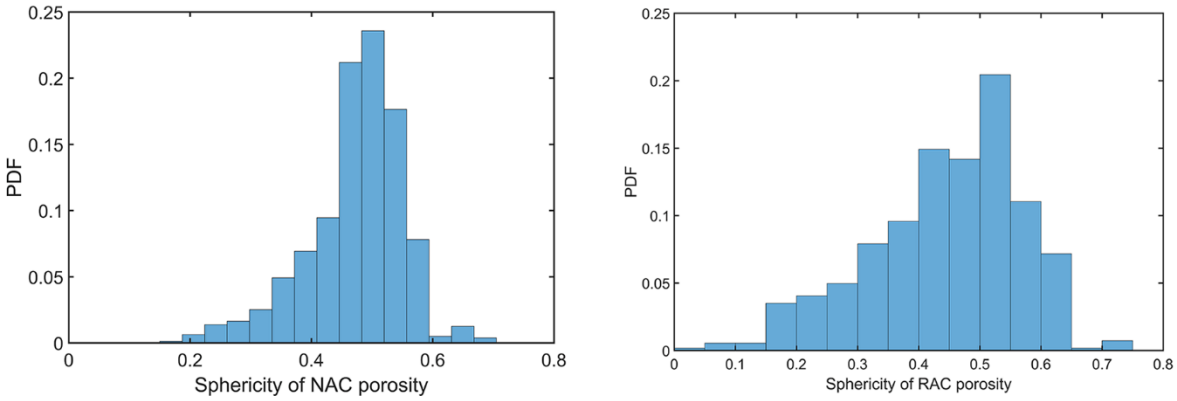

Fig. 41. Probability density functions of sphericity of NAC and RAC

5.5 Conclusion

With the aid of computational micromechanics and finite element method, factors associated with the wave modulus (WM) of elasticity evaluation are analyzed to investigate the microstructural origins on why WM is higher than its corresponding static modulus of elasticity. Possible factors (aggregate and void) are analyzed and discussed. While higher aggregate concentration results in an increase of both WM and static modulus of elasticity, it does not indicate that WM is more sensitive to aggregates than static modulus of elasticity. It is also noted that the presence of wave scattering and refraction around aggregates tends to result in lower WM when compared with the static cases. Microstructural porosity due to spherical voids leads to lower WM than the static modulus of elasticity of concrete. However, the crack-like voids prove to be the critical factor causing the higher WM. The crack-like voids are identified with a specific roundness or sphericity.

Chapter 6 Summary and Future Research

Based on the fundamentals of elastodynamics, the first main study focuses on elastography mapping. Resultantly, three elastography methods have been developed, considering external responses, data process of deep learning and untangling shear-compressional deformation, respectively. Validations show that these methods have the ability imaging elastography accurately. The common advantage of the three methods are free of frequency dependence. The integration method makes full use of CT image, which sheds light on those imaging devices that don't have the function of mechanical detection. The deep learning architecture greatly reduces the computation time of inverse analysis for the integration method. The deformation untangled method makes elastography more general and applicable without the limit of pure shear deformation.

The second main effort has been put in the investigation how microstructures affect the wave motion in composite materials. In this part, a question confusing researcher for more than half century has been clearly answered, why wave modulus is higher than its static counterpart. Finally, the crack-like voids prove to be the critical factor causing the higher WM.

In the future, deep learning based elastography will be studied furtherly and combined with the untangling algorithm for improving efficiency and removing noise. In addition, the physical relationship between WM and its static counterpart requires in-depth investigation based on computational mechanics.

REFERENCES

[1] J. M. B. Jerrold T. Bushberg, J. Anthony Seibert, Edwin M. Leidholdt, *The Essential Physics of Medical Imaging*, 3rd ed. Philadeiphia: Lippincott Williams & Wilkins, 2011.

[2] R. Nick Bryan, *Introduction to the Science of Medical Imaging*. Cambridge University Press, 2010.

[3] D. T. Ginat and R. Gupta, "Advances in Computed Tomography Imaging Technology," *Annu. Rev. Biomed. Eng*, vol. 16, pp. 431–53, 2014.

[4] R. J. Parmee, C. M. Collins, W. I. Milne, and M. T. Cole, "X-ray generation using carbon nanotubes," *Nano Converg.*, vol. 2, no. 1, p. 1, 2015.

[5] W. T. Sobol, "Recent advances in MRI technology: Implications for image quality and patient safety.," *Saudi J. Ophthalmol.*, vol. 26, no. 4, pp. 393–9, Oct. 2012.

[6] Z. Dong *et al.*, "Advances in MRI Techniques and Applications," *Biomed Res. Int.*, vol. 2015, pp. 1–2, 2015.

[7] J. H. Thrall, "Trends in Imaging Technology," *Radiology*, vol. 279, no. 3, 2016.

[8] G. Wang *et al.*, "Towards omni-tomography-grand fusion of multiple modalities for simultaneous interior tomography," *PLoS One*, vol. 7, no. 6, 2012.

[9] Y. Liu, L. Z. Sun, and G. Wang, "Tomography-based 3-D anisotropic elastography using boundary measurements," *IEEE Trans. Med. Imaging*, vol. 24, no. 10, pp. 1323–1333, 2005.

[10] Y. Liu, G. Wang, and L. Z. Sun, "Anisotropic elastography for local passive properties and active contractility of myocardium from dynamic heart imaging sequence," *Int. J. Biomed. Imaging*, vol. 2006, pp. 1–15, 2006.

[11] K. J. Parker, M. M. Doyley, and D. J. Rubens, “Imaging the elastic properties of tissue: the 20 year perspective,” *Phys. Med. Biol.*, vol. 57, pp. 5359–5360, 2012.

[12] F. A. Duck, *Physical properties of tissue: a comprehensive reference book*. Academic Press, 1990.

[13] Y. K. Mariappan, K. J. Glaser, and Richard L Ehman, “Magnetic Resonance Elastography: a Review,” *Clin. Anat.*, vol. 23, no. 5, pp. 497–511, 2010.

[14] J. Ophir, I. Cespedes, H. Ponnekanti, Y. Yazdi, and X. Li, “Elastography: A quantitative method for imaging the elasticity of biological tissues,” *Ultrason. Imaging*, vol. 13, no. 2, pp. 111–134, 1991.

[15] B. S. Garra *et al.*, “Elastography of breast lesions: initial clinical results.,” *Radiology*, vol. 202, no. 1, pp. 79–86, Jan. 1997.

[16] T. Faruk, M. K. Islam, S. Arefin, and M. Z. Haq, “The Journey of Elastography: Background, Current Status, and Future Possibilities in Breast Cancer Diagnosis,” *Clin. Breast Cancer*, vol. 15, no. 5, pp. 313–324, Oct. 2015.

[17] R. G. Barr, “Elastography in Clinical Practice,” *Radiol. Clin. North Am.*, vol. 52, no. 6, pp. 1145–1162, Nov. 2014.

[18] D. Liu, Z. Hu, G. Wang, and L. Sun, “Sound Transmission-Based Elastography Imaging,” *IEEE Access*, vol. 7, pp. 74383–74392, 2019.

[19] R. G. Barr, “Sonographic breast elastography: a primer.,” *J. Ultrasound Med.*, vol. 31, no. 5, pp. 773–83, May 2012.

[20] R. G. Barr, “US Elastography: Applications in Tumors,” in *Functional Imaging in Oncology*, Berlin, Heidelberg: Springer Berlin Heidelberg, 2014, pp. 459–488.

[21] P. G. M. de Jong, T. Arts, A. P. G. Hoeks, and R. S. Reneman, “Determination of Tissue

Motion Velocity by Correlation Interpolation of Pulsed Ultrasonic Echo Signals," *Ultrason. Imaging*, vol. 12, no. 2, pp. 84–98, Apr. 1990.

[22] F. Kallel and M. Bertrand, "A note on strain estimation using correlation techniques [tissue]," in *Proceedings of IEEE Ultrasonics Symposium*, 1993, pp. 883–887.

[23] H. Chen, H. Shi, and T. Varghese, "Improvement of elastographic displacement estimation using a two-step cross-correlation method," *Ultrasound Med. Biol.*, vol. 33, no. 1, pp. 48–56, 2007.

[24] D. S. Bell, J. C. Bamber, and R. J. Eckersley, "Segmentation and analysis of colour Doppler images of tumour vasculature," *Ultrasound Med. Biol.*, vol. 21, no. 5, pp. 635–647, Jan. 1995.

[25] T. Varghese, J. Ophir, and I. Céspedes, "Noise reduction in elastograms using temporal stretching with multicompression averaging," *Ultrasound Med. Biol.*, vol. 22, no. 8, pp. 1043–1052, Jan. 1996.

[26] T. Varghese and J. Ophir, "An analysis of elastographic contrast-to-noise ratio," *Ultrasound Med. Biol.*, vol. 24, no. 6, pp. 915–924, 1998.

[27] L. Sandrin *et al.*, "Transient elastography: a new noninvasive method for assessment of hepatic fibrosis.," *Ultrasound Med. Biol.*, vol. 29, no. 12, pp. 1705–1713, 2003.

[28] J.-L. Gennisson, T. Deffieux, M. Fink, and M. Tanter, "Ultrasound elastography: Principles and techniques," *Diagn. Interv. Imaging*, vol. 94, no. 5, pp. 487–495, 2013.

[29] A. Evans *et al.*, "Quantitative shear wave ultrasound elastography: initial experience in solid breast masses," *Breast Cancer Res.*, vol. 12, no. 6, p. R104, 2010.

[30] J. Bamber *et al.*, "EFSUMB Guidelines and Recommendations on the Clinical Use of Ultrasound Elastography. Part 1: Basic Principles and Technology," *Ultraschall der*

Medizin - Eur. J. Ultrasound, vol. 34, no. 02, pp. 169–184, Apr. 2013.

[31] S.-J. Hsu, "Acoustic Radiation Force and Elasticity Imaging," *J. Med. Ultrasound*, vol. 24, no. 1, pp. 1–2, 2016.

[32] K. R. Nightingale, M. L. Palmeri, R. W. Nightingale, and G. E. Trahey, "On the feasibility of remote palpation using acoustic radiation force.," *J. Acoust. Soc. Am.*, vol. 110, no. 1, pp. 625–34, 2001.

[33] B. S. Garra, "Elastography: history, principles, and technique comparison," *Abdom. Imaging*, vol. 40, no. 4, pp. 680–697, 2015.

[34] K. Nakashima *et al.*, "JSUM ultrasound elastography practice guidelines: breast," *J. Med. Ultrason.*, vol. 40, no. 4, pp. 359–391, Oct. 2013.

[35] D. T. Ginat, S. V. Destounis, R. G. Barr, B. Castaneda, J. G. Strang, and D. J. Rubens, "US Elastography of Breast and Prostate Lesions1," *RadioGraphics*, vol. 29, no. 7, pp. 2007–2016, Nov. 2009.

[36] A. Itoh *et al.*, "Breast Disease: Clinical Application of US Elastography for Diagnosis," *Radiology*, vol. 239, no. 2, pp. 341–350, May 2006.

[37] W. A. Berg *et al.*, "Shear-wave Elastography Improves the Specificity of Breast US: The BE1 Multinational Study of 939 Masses," *Radiology*, vol. 262, no. 2, pp. 435–449, Feb. 2012.

[38] A. Evans *et al.*, "Invasive Breast Cancer: Relationship between Shear-wave Elastographic Findings and Histologic Prognostic Factors," *Radiology*, vol. 263, no. 3, pp. 673–677, Jun. 2012.

[39] T. Varghese, J. . Zagzebski, and F. . Lee, "Elastographic imaging of thermal lesions in the liver in vivo following radiofrequency ablation: preliminary results," *Ultrasound*

Med. Biol., vol. 28, no. 11, pp. 1467–1473, 2002.

[40] Y. Kumashiro *et al.*, "Living donor liver transplantation for giant hepatic hemangioma with Kasabach-Merritt syndrome with a posterior segment graft," *Liver Transplant.*, vol. 8, no. 8, pp. 721–724, Aug. 2002.

[41] G. Ferraioli, C. Tinelli, B. Dal Bello, M. Zicchetti, G. Filice, and C. Filice, "Accuracy of real-time shear wave elastography for assessing liver fibrosis in chronic hepatitis C: A pilot study," *Hepatology*, vol. 56, no. 6, pp. 2125–2133, Dec. 2012.

[42] É. Bavu *et al.*, "Noninvasive In Vivo Liver Fibrosis Evaluation Using Supersonic Shear Imaging: A Clinical Study on 113 Hepatitis C Virus Patients," *Ultrasound Med. Biol.*, vol. 37, no. 9, pp. 1361–1373, 2011.

[43] M. Friedrich-Rust *et al.*, "Liver Fibrosis in Viral Hepatitis: Noninvasive Assessment with Acoustic Radiation Force Impulse Imaging versus Transient Elastography," *Radiology*, vol. 252, no. 2, pp. 595–604, Aug. 2009.

[44] Y. E. Chon *et al.*, "Performance of Transient Elastography for the Staging of Liver Fibrosis in Patients with Chronic Hepatitis B: A Meta-Analysis," *PLoS One*, vol. 7, no. 9, p. e44930, Sep. 2012.

[45] A. Lorenz *et al.*, "Ultrasonic tissue characterization-assessment of prostate tissue malignancy in vivo using a conventional classifier based tissue classification approach and elastographic imaging," in *2000 IEEE Ultrasonics Symposium. Proceedings. An International Symposium (Cat. No.00CH37121)*, 2000, vol. 2, pp. 1845–1848.

[46] R. Souchon *et al.*, "Visualisation of HIFU lesions using elastography of the human prostate in vivo: preliminary results," *Ultrasound Med. Biol.*, vol. 29, no. 7, pp. 1007–

1015, 2003.

[47] R. G. Barr, R. Memo, and C. R. Schaub, “Shear Wave Ultrasound Elastography of the Prostate,” *Ultrasound Q.*, vol. 28, no. 1, pp. 13–20, Mar. 2012.

[48] J. Bojunga, E. Herrmann, G. Meyer, S. Weber, S. Zeuzem, and M. Friedrich-Rust, “Real-Time Elastography for the Differentiation of Benign and Malignant Thyroid Nodules: A Meta-Analysis,” *Thyroid*, vol. 20, no. 10, pp. 1145–1150, Oct. 2010.

[49] D. S. Cooper *et al.*, “Revised American Thyroid Association Management Guidelines for Patients with Thyroid Nodules and Differentiated Thyroid Cancer,” *THYROID*, vol. 19, no. 11, 2009.

[50] C. Asteria *et al.*, “US-Elastography in the Differential Diagnosis of Benign and Malignant Thyroid Nodules,” *Thyroid*, vol. 18, no. 5, pp. 523–531, May 2008.

[51] A. C. Silva and M. D. Beland, “Special Section Introduction: Elastography,” *Abdom. Imaging*, vol. 40, no. 4, p. 679, 2015.

[52] J. B. Fowlkes *et al.*, “Magnetic-resonance imaging techniques for detection of elasticity variation,” *Med. Phys.*, vol. 22, no. 11, p. 1771, 1995.

[53] J. Bishop, G. Poole, M. Leitch, and D. B. Plewes, “Magnetic resonance imaging of shear wave propagation in excised tissue,” *J. Magn. Reson. Imaging*, vol. 8, no. 6, pp. 1257–1265, Nov. 1998.

[54] P. A. Hardy, A. C. Ridler, C. B. Chiarot, D. B. Plewes, and R. M. Henkelman, “Imaging articular cartilage under compression--cartilage elastography.,” *Magn. Reson. Med.*, vol. 53, no. 5, pp. 1065–73, May 2005.

[55] R. Muthupillai, D. J. Lomas, P. J. Rossman, J. F. Greenleaf, A. Manduca, and R. L. Ehman, “Magnetic Resonance Elastography by Direct Visualization of Propagating Acoustic

Strain Waves," *Science*, vol. 269, no. 5232, pp. 1854–1857, 1995.

[56] G. Low, S. A. Kruse, and D. J. Lomas, "General review of magnetic resonance elastography," *World J. Radiol.*, vol. 8, no. 1, pp. 59–72, Jan. 2016.

[57] R. Sinkus, J. Lorenzen, D. Schrader, M. Lorenzen, M. Dargatz, and D. Holz, "High-resolution tensor MR elastography for breast tumour detection.," *Phys. Med. Biol.*, vol. 45, no. 6, pp. 1649–64, Jun. 2000.

[58] J. B. Weaver, E. E. W. Van Houten, M. I. Miga, F. E. Kennedy, and K. D. Paulsen, "Magnetic resonance elastography using 3D gradient echo measurements of steady-state motion," *Med. Phys.*, vol. 28, no. 8, pp. 1620–1628, 2001.

[59] S. K. Venkatesh and R. L. Ehman, "Magnetic resonance elastography of liver," *Magn. Reson. Imaging Clin. N. Am.*, vol. 22, no. 3, pp. 433–46, Aug. 2014.

[60] S. K. Venkatesh, M. Yin, and R. L. Ehman, "Magnetic resonance elastography of liver: technique, analysis, and clinical applications," *J. Magn. Reson. imaging*, vol. 37, no. 3, pp. 544–55, Mar. 2013.

[61] L. Huwart *et al.*, "Liver Fibrosis: Noninvasive Assessment with MR Elastography versus Aspartate Aminotransferase–to-Platelet Ratio Index," *Radiology*, vol. 245, no. 2, pp. 458–466, Nov. 2007.

[62] S. K. Venkatesh *et al.*, "MR elastography of liver tumors: preliminary results.," *AJR. Am. J. Roentgenol.*, vol. 190, no. 6, pp. 1534–40, Jun. 2008.

[63] A. L. McKnight, J. L. Kugel, P. J. Rossman, A. Manduca, L. C. Hartmann, and R. L. Ehman, "MR Elastography of Breast Cancer: Preliminary Results," *Am. J. Roentgenol.*, vol. 178, pp. 1411–1417, 2002.

[64] R. Sinkus, M. Tanter, T. Xydeas, S. Catheline, J. Bercoff, and M. Fink, "Viscoelastic shear

properties of in vivo breast lesions measured by MR elastography," *Magn. Reson. Imaging*, vol. 23, no. 2, pp. 159–165, 2005.

[65] R. Sinkus, K. Siegmann, T. Xydeas, M. Tanter, C. Claussen, and M. Fink, "MR elastography of breast lesions: understanding the solid/liquid duality can improve the specificity of contrast-enhanced MR mammography," *Magn. Reson. Med.*, vol. 58, no. 6, pp. 1135–44, Dec. 2007.

[66] M. B. Barton, R. Harris, and S. W. Fletcher, "Does This Patient Have Breast Cancer? The Screening Clinical Breast Examination: Should It Be Done? How?," *JAMA*, vol. 282, no. 13, p. 1270, Oct. 1999.

[67] M. A. Dresner, G. H. Rose, P. J. Rossman, R. Muthupillai, A. Manduca, and R. L. Ehman, "Magnetic resonance elastography of skeletal muscle.," *J. Magn. Reson. imaging*, vol. 13, no. 2, pp. 269–76, Feb. 2001.

[68] J. R. Basford, T. R. Jenkyn, K.-N. An, R. L. Ehman, G. Heers, and K. R. Kaufman, "Evaluation of healthy and diseased muscle with magnetic resonance elastography," *Arch. Phys. Med. Rehabil.*, vol. 83, no. 11, pp. 1530–1536, 2002.

[69] S. I. Ringleb, S. F. Bensamoun, Q. Chen, A. Manduca, K.-N. An, and R. L. Ehman, "Applications of magnetic resonance elastography to healthy and pathologic skeletal muscle," *J. Magn. Reson. Imaging*, vol. 25, no. 2, pp. 301–9, Feb. 2007.

[70] I. Sack, J. Bernarding, and J. Braun, "Analysis of wave patterns in MR elastography of skeletal muscle using coupled harmonic oscillator simulations," *Magn. Reson. Imaging*, vol. 20, no. 1, pp. 95–104, 2002.

[71] L. Xu, Y. Lin, Z. N. Xi, H. Shen, and P. Y. Gao, "Magnetic Resonance Elastography of the Human Brain: A Preliminary Study," *Acta radiol.*, vol. 48, no. 1, pp. 112–115, Jan.

2007.

[72] S. A. Kruse *et al.*, "Magnetic resonance elastography of the brain," *Neuroimage*, vol. 39, no. 1, pp. 231–237, 2008.

[73] A. Zorgani *et al.*, "Brain palpation from physiological vibrations using MRI," *Proc. Natl. Acad. Sci.*, vol. 112, no. 42, pp. 12917–12921, 2015.

[74] P. J. McCracken, A. Manduca, J. Felmlee, and R. L. Ehman, "Mechanical transient-based magnetic resonance elastography," *Magn. Reson. Med.*, vol. 53, no. 3, pp. 628–39, Mar. 2005.

[75] J. B. Weaver *et al.*, "Brain mechanical property measurement using MRE with intrinsic activation," *Phys. Med. Biol.*, vol. 57, no. 22, pp. 7275–87, 2012.

[76] S. Zhao, A. Jackson, and G. J. Parker, "Auto-elastography of the brain," in *Proc. Intl. Soc. Mag. Reson. Med.*, 2009, p. 713.

[77] A. J. Pattison, I. M. Perreard, J. B. Weaver, and K. D. Paulsen, "Poroelastic MRE reconstructions of brain acquired with intrinsic activation," in *Proc. Intl. Soc. Mag. Reson. Med.*, 2010, p. 3404.

[78] R. E. Philleo, "Comparison of results of three methods for determining Young's modulus of elasticity of concrete," *ACI J. Proc.*, vol. 51, pp. 461–469, 1955.

[79] D. N. Nwokoye, "Assesssment of the elatic moduli of cement paste and mortar phases in concrete from pulse velocity tests," *Cem. Concr. Res.*, vol. 4, pp. 641–655, 1974.

[80] S. Popovics, J. L. Rose, and J. S. Popovics, "The behaviour of ultrasonic pulses in concrete," *Cem. Concr. Res.*, vol. 20, no. 2, pp. 259–270, 1990.

[81] G. Song, H. Gu, and Y.-L. Mo, "Smart aggregates: multi-functional sensors for concrete structures—a tutorial and a review," *Smart Mater. Struct.*, vol. 17, no. 3, p. 033001,

2008.

[82] P. Qiao and F. Chen, “Improved mechanical properties and early-age shrinkage resistance of recycled aggregate concrete with atomic polymer technology,” *J. Mater. Civ. Eng.*, vol. 25, no. 7, pp. 836–845, 2013.

[83] P. Qiao, “Seismic performance and smart health monitoring of concrete with recycled aggregate Part I: Smart health monitoring of concrete with recycled aggregate,” 2010.

[84] R. M. Lerner, S. R. Huang, and K. J. Parker, “‘Sonoelasticity’ images derived from ultrasound signals in mechanically vibrated tissues,” *Ultrasound Med. Biol.*, vol. 16, no. 3, pp. 231–239, Jan. 1990.

[85] J. Ophir, I. Céspedes, H. Ponnekanti, Y. Yazdi, and X. Li, “Elastography: A quantitative method for imaging the elasticity of biological tissues,” *Ultrason. Imaging*, vol. 13, no. 2, pp. 111–134, Apr. 1991.

[86] Y.-L. Liu *et al.*, “In vivo and ex vivo elastic properties of brain tissues measured with ultrasound elastography,” *J. Mech. Behav. Biomed. Mater.*, vol. 83, pp. 120–125, Jul. 2018.

[87] R. J. DeWall, “Ultrasound Elastography: Principles, Techniques, and Clinical Applications,” *Crit. Rev. Biomed. Eng.*, vol. 41, no. 1, pp. 1–19, 2013.

[88] U. Zaleska-Dorobisz, K. Kaczorowski, A. Pawlus, A. Puchalska, and M. Inglot, “Ultrasound elastography - review of techniques and its clinical applications.,” *Adv. Clin. Exp. Med.*, vol. 23, no. 4, pp. 645–655, 2014.

[89] T. Shiina, “Ultrasound elastography: Development of novel technologies and standardization,” *Jpn. J. Appl. Phys.*, vol. 53, no. 7 SPEC. ISSUE, 2014.

[90] R. M. S. Sigrist, J. Liau, A. El Kaffas, M. C. Chammas, and J. K. Willmann, "Ultrasound Elastography: Review of Techniques and Clinical Applications," *Theranostics*, vol. 7, no. 5, pp. 1303–1329, 2017.

[91] T. J. Hamilton *et al.*, "X-ray elastography: Modification of x-ray phase contrast images using ultrasonic radiation pressure," *J. Appl. Phys.*, vol. 105, no. 10, p. 102001, May 2009.

[92] K. J. Parker, J. Ormachea, F. Zvietcovich, and B. Castaneda, "Reverberant shear wave fields and estimation of tissue properties," *Phys. Med. Biol.*, vol. 62, no. 3, pp. 1046–1061, Feb. 2017.

[93] J. Racedo and M. W. Urban, "Evaluation of Reconstruction Parameters for Two-Dimensional Comb-push Ultrasound Shear Wave Elastography," *IEEE Trans. Ultrason. Ferroelectr. Freq. Control*, pp. 1–9, 2018.

[94] M. M. Doyley, "Model-based elastography: a survey of approaches to the inverse elasticity problem," *Phys. Med. Biol.*, vol. 57, no. 3, pp. R35–R73, Feb. 2012.

[95] K. F. Graff, *Wave Motion in Elastic Solids*. New York: Dover Publications, 1991.

[96] E. E. W. Van Houten, M. I. Miga, J. B. Weaver, F. E. Kennedy, and K. D. Paulsen, "Three-dimensional subzone-based reconstruction algorithm for MR elastography," *Magn. Reson. Med.*, vol. 45, no. 5, pp. 827–837, May 2001.

[97] S. Catheline, N. Benech, J. Brum, and C. Negreira, "Time Reversal of Elastic Waves in Soft Solids," *Phys. Rev. Lett.*, vol. 100, no. 6, p. 064301, Feb. 2008.

[98] J. Brum, S. Catheline, N. Benech, and C. Negreira, "Quantitative shear elasticity imaging from a complex elastic wavefield in soft solids with application to passive elastography," *IEEE Trans. Ultrason. Ferroelectr. Freq. Control*, vol. 62, no. 4, pp. 673–

685, Apr. 2015.

[99] A. P. Sarvazyan, O. V Rudenko, S. D. Swanson, J. B. Fowlkes, and S. Y. Emelianov, "Shear wave elasticity imaging: a new ultrasonic technology of medical diagnostics," *Ultrasound Med. Biol.*, vol. 24, no. 9, pp. 1419–1435, Dec. 1998.

[100] J. Bercoff, M. Tanter, and M. Fink, "Supersonic shear imaging: a new technique for soft tissue elasticity mapping," *IEEE Trans. Ultrason. Ferroelectr. Freq. Control*, vol. 51, no. 4, pp. 396–409, Apr. 2004.

[101] L. Ji, J. R. McLaughlin, D. Renzi, and J.-R. Yoon, "Interior elastodynamics inverse problems: shear wave speed reconstruction in transient elastography," *Inverse Probl.*, vol. 19, no. 6, pp. S1–S29, Dec. 2003.

[102] K. J. Parker, S. R. Huang, R. A. Musulin, and R. M. Lerner, "Tissue response to mechanical vibrations for 'sonoelasticity imaging,'" *Ultrasound Med. Biol.*, vol. 16, no. 3, pp. 241–246, Jan. 1990.

[103] Y. Liu, G. Wang, and L. Z. Sun, "Elastography Method to Identify Material Distribution in Two-Phase Nonlinear Media," *J. Eng. Mech.*, vol. 140, no. 5, p. 04014010, 2014.

[104] Z. Yuan, H. Zhao, C. Wu, Q. Zhang, and H. Jiang, "Finite-element-based photoacoustic tomography: phantom and chicken bone experiments," *Appl. Opt.*, vol. 45, no. 13, p. 3177, 2006.

[105] T. Kitazaki, K. Kondo, M. Yamakawa, and T. Shiina, "Shear wavelength estimation based on inverse filtering and multiple-point shear wave generation," *Jpn. J. Appl. Phys*, vol. 55, pp. 7–10, 2016.

[106] F. J. Serón, F. J. Sanz, M. Kindelán, and J. I. Badal, "Finite-element method for elastic wave propagation," *Commun. Appl. Numer. Methods*, vol. 6, no. 5, pp. 359–368, Jul.

1990.

[107] D. C. Montgomery, *Design And Analysis Of Experiments*, 5th ed. John Wiley & Sons, Inc., 2000.

[108] P. J. Ross, *Taguchi techniques for quality engineering*, 2nd ed. McGraw-Hill, 1996.

[109] S. Budday *et al.*, "Mechanical characterization of human brain tissue," *Acta Biomater.*, vol. 48, pp. 319–340, 2017.

[110] K. J. Keesman, *System Identification: An Introduction*. London: Springer, 2011.

[111] J. T. Bushberg *et al.*, *The Essential Physics of Medical Imaging*, 3rd ed. Philadelphia: Lippincott Williams & Wilkins, 2012.

[112] M. C. Murphy, A. Manduca, J. D. Trzasko, K. J. Glaser, J. Huston, and R. L. Ehman, "Artificial neural networks for stiffness estimation in magnetic resonance elastography," *Magn. Reson. Med.*, vol. 80, no. 1, pp. 351–360, Jul. 2018.

[113] J. Yoo, A. Wahab, and J. C. Ye, "A Mathematical Framework for Deep Learning in Elastic Source Imaging," *arXiv:1802.10055*, pp. 1–24, 2018.

[114] B. J. Erickson, P. Korfiatis, Z. Akkus, and T. L. Kline, "Machine Learning for Medical Imaging," *Radiographics*, vol. 37, no. 2, pp. 505–515, 2017.

[115] A. Krizhevsky, I. Sutskever, and G. E. Hinton, "ImageNet Classification with Deep Convolutional Neural Networks," in *25th International Conference on Neural Information Processing Systems*, 2012, pp. 1097–1105.

[116] J. Schmidhuber, "Deep Learning in neural networks: An overview," *Neural Networks*, vol. 61. Elsevier Ltd, pp. 85–117, 01-Jan-2015.

[117] D. M. Pelt and J. A. Sethian, "A mixed-scale dense convolutional neural network for image analysis," *Proc. Natl. Acad. Sci.*, vol. 115, no. 2, pp. 254–259, 2018.

[118] Y. Bengio, A. Courville, and P. Vincent, “Representation learning: A review and new perspectives,” *IEEE Trans. Pattern Anal. Mach. Intell.*, vol. 35, no. 8, pp. 1798–1828, 2013.

[119] I. Goodfellow, Y. Bengio, and A. Courvile, *Deep learning*. MIT Press, 2016.

[120] A. Ameri, M. A. Akhaee, E. Scheme, and K. Englehart, “Regression convolutional neural network for improved simultaneous EMG control,” *J. Neural Eng.*, vol. 16, no. 3, Apr. 2019.

[121] D. Verstraete, A. Ferrada, E. L. Droguett, V. Meruane, and M. Modarres, “Deep learning enabled fault diagnosis using time-frequency image analysis of rolling element bearings,” *Shock Vib.*, vol. 2017, 2017.

[122] X. Fu, C. Zhang, X. Peng, L. Jian, and Z. Liu, “Towards end-to-end pulsed eddy current classification and regression with CNN,” *2019 IEEE Int. Instrum. Meas. Technol. Conf.*, pp. 1–5, Sep. 2019.

[123] C. Szegedy *et al.*, “Going deeper with convolutions,” *Proc. IEEE Comput. Soc. Conf. Comput. Vis. Pattern Recognit.*, vol. 07-12-June, pp. 1–9, Oct. 2015.

[124] D. P. Kingma and J. Ba, “Adam: A Method for Stochastic Optimization,” *arXiv: 1412.6980*, Dec. 2014.

[125] A. J. McDonald, “Solid Rocket Motor Failure,” in *Encyclopedia of Aerospace Engineering*, New York: Wiley, 2010.

[126] A. Q. Le, L. Z. Sun, and T. C. Miller, “Detectability of Delaminations in Solid Rocket Motors with Embedded Stress Sensors,” *J. Propuls. Power*, vol. 29, no. 2, pp. 299–304, 2013.

[127] D. Dhital, J. R. Lee, C. Farrar, and D. Mascarenas, “A review of flaws and damage in

space launch vehicles: Motors and engines," *J. Intell. Mater. Syst. Struct.*, vol. 25, no. 5, pp. 524–540, Mar. 2014.

[128] T. S. Sojourner, D. E. Richardson, B. D. Allen, K. S. McHenry, and B. E. Goldberg, "Solid rocket booster reliability and historical failure modes review," *51st AIAA/SAE/ASEE Jt. Propuls. Conf.*, pp. 1–17, 2015.

[129] A. Q. Le, L. Z. Sun, and T. C. Miller, "Health Monitoring and Diagnosis of Solid Rocket Motors with Bore Cracks," *J. Aerosp. Eng.*, vol. 29, no. 3, p. 04015058, 2015.

[130] G. Tussiwand, "Application of Embedded Sensors Technology to a Full-Scale Nozzleless Rocket Motor," *43rd AIAA/ASME/SAE/ASEE Jt. Propuls. Conf. Exhib.*, Jul. 2007.

[131] G. Reeling Brouwer, A. Pfiffer, and L. Bancallari, "Development and deployment of diagnostic prognostic tactical solid rocket motor demonstrator," *47th AIAA/ASME/SAE/ASEE Jt. Propuls. Conf. & Exhib.*, Jul. 2011.

[132] G. A. Ruderman, "Health Management Issues and Strategy for Air Force Missiles," *Proc. First Int. Forum Integr. Syst. Heal. Eng.*, pp. 7–10, 2005.

[133] H. Chelner, "Embedded sensor technology for solid rocket motor health monitoring," Huntsville, Alabama, 2003.

[134] J. Buswell and A. Fall, "Lessons learned from health monitoring of rocket motors," *41st AIAA/ASME/SAE/ASEE Jt. Propuls. Conf. Exhib.*, no. July, pp. 1–12, 2005.

[135] C. Riziotis, L. Eineder, L. Bancallari, and G. Tussiwand, "Fiber optic architectures for strain monitoring of solid rocket motors' propellant," *Sens. Lett.*, vol. 11, no. 8, pp. 1403–1407, 2013.

[136] E. C. Sengezer and G. D. Seidel, "Structural health monitoring of nanocomposite

bonded energetic materials through piezoresistive response," *AIAA J.*, vol. 56, no. 3, pp. 1225–1238, 2018.

[137] N. Shirodkar, S. Rocker, and G. D. Seidel, "Structural health monitoring of solid rocket propellants using piezoresistive properties of dispersed carbon nano-tube sensing networks," *ASME 2018 Conf. Smart Mater. Adapt. Struct. Intell. Syst. SMASIS 2018*, vol. 1, 2018.

[138] C. Lopatin and D. Grinstein, "Active sensing for monitoring the properties of solid rocket motor propellant grains," *Propellants, Explos. Pyrotech.*, vol. 40, no. 2, pp. 295–302, Apr. 2015.

[139] D. Izzo, M. Märtens, and B. Pan, "A survey on artificial intelligence trends in spacecraft guidance dynamics and control," *Astrodynamics*, vol. 3, no. 4, pp. 287–299, Dec. 2019.

[140] M. Schwabacher, "Machine learning for rocket propulsion health monitoring," *SAE Tech. Pap.*, pp. 2005-01–3370, 2005.

[141] H. H. Dewey and D. R. Devries, "Case study in utilizing the Internet of Things as a PHM architecture for aerospace applications," *IEEE Aerosp. Conf. Proc.*, vol. 2018-March, pp. 1–15, 2018.

[142] Y. Cao, W. Huang, and J. Li, "Effect of ambient vibration on solid rocket motor grain and propellant/liner bonding interface," in *AIP Conference Proceedings*, 2017, vol. 1839, p. 020078.

[143] R. Marimuthu and B. Nageswara Rao, "Development of efficient finite elements for structural integrity analysis of solid rocket motor propellant grains," *Int. J. Press. Vessel. Pip.*, vol. 111–112, pp. 131–145, Nov. 2013.

[144] A. Manduca *et al.*, "Magnetic resonance elastography: Non-invasive mapping of tissue elasticity," *Med. Image Anal.*, vol. 5, no. 4, pp. 237–254, 2001.

[145] Y. Cao, Y. Zheng, G. Y. Li, and Y. Jiang, "Elastodiagnosis of diseases: A review," *Extreme Mechanics Letters*, vol. 27. Elsevier Ltd, pp. 102–123, 01-Feb-2019.

[146] E. B. Tapper and R. Loomba, "Noninvasive imaging biomarker assessment of liver fibrosis by elastography in NAFLD," *Nat. Rev. Gastroenterol. Hepatol.*, vol. 15, no. 5, pp. 274–282, 2018.

[147] B. F. Kennedy, P. Wijesinghe, and D. D. Sampson, "The emergence of optical elastography in biomedicine," *Nat. Photonics*, vol. 11, no. 4, pp. 215–221, 2017.

[148] S. Ghosh *et al.*, "Deformation Microscopy for Dynamic Intracellular and Intranuclear Mapping of Mechanics with High Spatiotemporal Resolution," *Cell Rep.*, vol. 27, no. 5, pp. 1607–1620, 2019.

[149] N. Leartprapun, R. R. Iyer, G. R. Untracht, J. A. Mulligan, and S. G. Adie, "Photonic force optical coherence elastography for three-dimensional mechanical microscopy," *Nat. Commun.*, vol. 9, no. 1, pp. 1–13, 2018.

[150] S. Patz *et al.*, "Imaging localized neuronal activity at fast time scales through biomechanics," *Sci. Adv.*, vol. 5, no. 4, 2019.

[151] P. Kennedy *et al.*, "Quantitative Elastography Methods in Liver Disease: Current Evidence and Future Directions," *Radiology*, vol. 286, no. 3, pp. 738–763, 2018.

[152] E. Herrmann *et al.*, "Assessment of biopsy-proven liver fibrosis by two-dimensional shear wave elastography: An individual patient data-based meta-analysis," *Hepatology*, vol. 67, no. 1, pp. 260–272, 2018.

[153] M. Friedrich-Rust, T. Poynard, and L. Castera, "Critical comparison of elastography

methods to assess chronic liver disease," *Nat. Rev. Gastroenterol. Hepatol.*, vol. 13, no. 7, pp. 402–411, 2016.

[154] A. Malandrino, M. Mak, R. D. Kamm, and E. Moeendarbary, "Complex mechanics of the heterogeneous extracellular matrix in cancer," *Extreme Mechanics Letters*, vol. 21. Elsevier Ltd, pp. 25–34, 01-May-2018.

[155] T. Deffieux, J.-L. Gennisson, J. Bercoff, and M. Tanter, "On the effects of reflected waves in transient shear wave elastography," *IEEE Trans. Ultrason. Ferroelectr. Freq. Control*, vol. 58, no. 10, pp. 2032–2035, Oct. 2011.

[156] A. Manduca, D. S. Lake, S. A. Kruse, and R. L. Ehman, "Spatio-temporal directional filtering for improved inversion of MR elastography images," *Med. Image Anal.*, vol. 7, pp. 465–473, 2003.

[157] S. W. Gordon-Wylie *et al.*, "MR elastography at 1 Hz of gelatin phantoms using 3D or 4D acquisition," *J. Magn. Reson.*, vol. 296, pp. 112–120, Nov. 2018.

[158] J. Cui *et al.*, "Magnetic resonance elastography is superior to acoustic radiation force impulse for the Diagnosis of fibrosis in patients with biopsy-proven nonalcoholic fatty liver disease: A prospective study," *Hepatology*, vol. 63, no. 2, pp. 453–461, 2016.

[159] P. Qiao, W. Fan, and F. Chen, "Material property assessment and crack identification of recycled concrete with embedded smart cement modules," in *Proceedings of SPIE - The International Society for Optical Engineering*, 2011, vol. 7981, pp. 1–13.

[160] L. Qixian and J. H. Bungey, "Using compression wave ultrasonic transducers to measure the velocity of surface waves and hence determine dynamic modulus of elasticity for concrete," *Constr. Build. Mater.*, vol. 10, no. 4, pp. 237–242, 1996.

[161] M. Sun, W. J. Staszewski, R. N. Swamy, and Z. Li, "Application of low-profile piezoceramic transducers for health monitoring of concrete structures," *NDT E Int.*, vol. 41, pp. 589–595, 2008.

[162] J. Zheng, X. Zhou, and L. Sun, "Analytical prediction of the Young's modulus of concrete with spheroidal aggregates," *J. Mater. Civ. Eng.*, vol. 28, no. 1, p. 04015080, Jan. 2016.

[163] G. Li, Y. Zhao, S.-S. Pang, and Y. Li, "Effective Young's modulus estimation of concrete," *Cem. Concr. Res.*, vol. 29, no. 9, pp. 1455–1462, Sep. 1999.

[164] R. Rezakhani, X. Zhou, and G. Cusatis, "Adaptive multiscale homogenization of the lattice discrete particle model for the analysis of damage and fracture in concrete," *Int. J. Solids Struct.*, vol. 125, pp. 50–67, Oct. 2017.

[165] R.-B. Yang, "A dynamic generalized self-consistent model for wave propagation in particulate composites," *J. Appl. Mech.*, vol. 70, no. 4, pp. 575–582, 2003.

[166] J.-F. Chaix, M. Rossat, V. Garnier, and G. Corneloup, "An experimental evaluation of two effective medium theories for ultrasonic wave propagation in concrete," *J. Acoust. Soc. Am.*, vol. 131, no. 6, pp. 4481–4490, 2012.

[167] T. Planès and E. Larose, "A review of ultrasonic coda wave interferometry in concrete," *Cem. Concr. Res.*, vol. 53, pp. 248–255, 2013.

[168] C. Kohlhauser and C. Hellmich, "Ultrasonic contact pulse transmission for elastic wave velocity and stiffness determination: Influence of specimen geometry and porosity," *Eng. Struct.*, vol. 47, pp. 115–133, Feb. 2013.

[169] A. Zaoui, "Continuum Micromechanics: Survey," *J. Eng. Mech.*, vol. 128, no. 8, pp. 808–816, 2002.

[170] P. P. Smolarkiewicz, C. L. Nogueira, and K. J. Willam, “Ultrasonic evaluation damage in heterogeneous concrete materials,” in *European Congress on Computational Methods in Applied Sciences and Engineering (ECCOMAS 2000)*, 2000, no. September, pp. 1–13.

[171] J.-K. Kim, J. Woo, and W.-B. Na, “Finite element simulation of two-point elastic wave excitation method for damage detection in concrete structures,” *Russ. J. Nondestruct. Test.*, vol. 44, no. 10, pp. 719–726, 2008.

[172] G. Acciani, G. Fornarelli, A. Giaquinto, and D. Maiullari, “Nondestructive evaluation of defects in concrete structures based on finite element simulations of ultrasonic wave propagation,” *Nondestruct. Test. Eval.*, vol. 25, no. 4, pp. 289–315, 2010.

[173] M. B. Leite and P. J. M. Monteiro, “Microstructural analysis of recycled concrete using X-ray microtomography,” *Cem. Concr. Res.*, vol. 81, pp. 38–48, Mar. 2016.

[174] Q. Luo, D. Liu, P. Qiao, Q. Feng, and L. Sun, “Microstructural damage characterization of concrete under freeze-thaw action,” *Int. J. Damage Mech.*, vol. 27, no. 10, pp. 1551–1568, 2018.

[175] Q. Luo, D. Liu, P. Qiao, Z. Zhou, Y. Zhao, and L. Sun, “Micro-CT-based micromechanics and numerical homogenization for effective elastic property of ultra-high performance concrete,” *Int. J. Damage Mech.*, vol. 29, no. 1, pp. 45–66, Jan. 2020.

[176] B. Budiansky and R. J. O’connell, “Elastic moduli of a cracked solid,” *Int. J. Solids Struct.*, vol. 12, no. 2, pp. 81–97, 1976.

[177] L. Dormieux and D. Kondo, “Stress-based estimates and bounds of effective elastic properties: The case of cracked media with unilateral effects,” *Comput. Mater. Sci.*, vol. 46, no. 1, pp. 173–179, Jul. 2009.

[178] H. H. Pan, Y. W. Liu, and F. Y. Wu, “Effect of micro-and nano-cracks for the mechanical

properties of cementitious materials," in *Proceedings of 4th International Conference on Construction Materials*, 2009, pp. 1141–1147.

[179] S.-T. Nguyen, "Effect of pore shape on the effective behavior of viscoelastic porous media," *Int. J. Solids Struct.*, vol. 125, pp. 161–171, Oct. 2017.

[180] D. Shuai, J. Wei, B. Di, and P. Ding, "Theoretical and experimental research on elastic wave velocity influenced by crack aperture," in *SPG/SEG 2016 International Geophysical Conference*, 2016, pp. 600–602.

[181] L. Wang *et al.*, "Influence of pores on crack initiation in monotonic tensile and cyclic loadings in lost foam casting A319 alloy by using 3D in-situ analysis," *Mater. Sci. Eng. A*, vol. 673, pp. 362–372, Sep. 2016.

[182] ASTM (American Society for Testing and Materials), *Standard Test Method for Static Modulus of Elasticity and Poisson's Ratio of Concrete in Compression*. West Conshohocken, PA: ASTM C469/C469M-14, 2014.

[183] M. Irfan-ul-Hassan, B. Pichler, R. Reihsner, and C. Hellmich, "Elastic and creep properties of young cement paste, as determined from hourly repeated minute-long quasi-static tests," *Cem. Concr. Res.*, vol. 82, pp. 36–49, Apr. 2016.

[184] M. Ausweger *et al.*, "Early-Age Evolution of Strength, Stiffness, and Non-Aging Creep of Concretes: Experimental Characterization and Correlation Analysis," *Materials (Basel).*, vol. 12, no. 2, p. 207, Jan. 2019.

[185] M. Alger, *Polymer Science Dictionary*, Third. Dordrecht: Springer, 2017.